

Progressive numerical model validation of a bowstring-arch railway bridge based on a structural health monitoring system

Andreia Meixedo^{1*}, Diogo Ribeiro², João Santos³, Rui Calçada⁴, Michael Todd⁵

ABSTRACT

This paper presents a progressive numerical model validation of a bowstring-arch railway bridge based on the analysis of experimental data from different structural response measurements, namely, static deformations under environmental actions, modal vibrations, and transient dynamic responses under traffic loads. This work also addresses an integrated approach that uses structural health monitoring (SHM) measurements in combination with FE modelling to understand the structural behaviour of a long-span complex bridge. An *in-situ*, progressively-phased SHM system has provided a diverse set of data streams ranging from static and dynamic responses to the measurement of environmental and operational traffic loads. The first phase consists of defining a detailed baseline finite element (FE) model of the bridge, envisaging the initial condition of the structure immediately after construction, and its validation using modal parameters (natural frequencies and mode shapes) derived from an ambient vibration test. Since in-service deflections generally do not exercise the non-linear regime of the response of the bridge, the second phase focuses on the analysis of static response data and temperature measurements to validate the non-linear behaviour of the structural system, particularly at the bearing devices, under slow actions. The third and final phase addresses the dynamic analysis under traffic actions, which provides greater sensitivity in the detection of non-linear behaviour due to the effects of high amplitude actions induced by regular train loading profiles. In order to guarantee the accuracy of the baseline numerical model, particularly under temperature and traffic actions, it was necessary to use contact restrictions in some specific bearing devices. This improvement is in line with the structural changes detected in some bearing devices through visual inspections. As a result, an updated numerical model capable of reproducing the modal, static, and dynamic structural responses was achieved, showing a very good agreement between experimental and numerical data. In future applications, this updated numerical model will be useful for assessing the condition of the bridge under traffic loads, namely to identify damages and support the adoption of life cycle maintenance strategies based on the integration of SHM systems with (stochastic) load and failure models.

Keywords: progressive model validation, railway bridge, structural health monitoring, non-linear behaviour, bearing devices, modal properties, environmental loads, traffic loads.

¹ PhD. Student, CONSTRUCT-LESE, Faculty of Engineering, University of Porto. ameixedo@fe.up.pt

² Adjunct Professor, CONSTRUCT-LESE, School of Engineering, Polytechnic of Porto. drr@isep.ipp.pt

³ Researcher, LNEC, Laboratório Nacional de Engenharia Civil. josantos@lneec.pt

⁴ Full Professor, CONSTRUCT-LESE, Faculty of Engineering, University of Porto. ruiabc@fe.up.pt

⁵ Full Professor, Department of Structural Engineering, University California San Diego, USA. mdtodd@ucsd.edu

1. Introduction

The large majority of bridges are assessed through periodic visual inspections; however, these are expensive, temporally inconsistent, and prone to human errors in judgment and interpretation, which ultimately led to the increasing development and deployment of structural health monitoring (SHM) systems, particularly for large newly built bridges [1]. These monitoring systems considerably increase the experimental data available for structural assessment [2]. With specific regard to railway bridges, the heavy moving loads imposed on these structures, typically for short periods of time, may be undesirable for fatigue or wear life, but can be considered an advantage for observing the full range of structural response behaviour, due to the high amplitude of traffic-induced vibrations [3]. An important complement and extension of SHM systems is the development and operation of well-validated numerical models to accurately reproduce and predict structural behaviour in order to assess structural damage and safety [4, 5].

Finite element (FE) numerical models with growing complexity have been instrumental to in correctly evaluating different phenomena that occur in railway bridges, such as the interaction between separate adjacent decks provided by the ballast layer [6], the coupling effect between successive spans [7], the non-linear behaviour at the track-deck interface [8], or the identification of damage in complex bridges [3]. An accurate and reliable assessment of the structural safety of railway bridges based on numerical models depends, however, on their experimental validation under environmental and traffic actions, and, in some situations, it may be necessary to update the model, which typically involves adjustments to specific parameters of the model to increase the correlation between numerical and experimental data [9–11]. Numerous works that address model validation can be found in the literature, using not only direct measurements under static and dynamic loads, such as strains, displacements and accelerations [12,13], but also, and more commonly, modal information, such as natural frequencies, damping and mode shapes based on acceleration measurements [10,14–16]. Tomé et al. [17] showed the need to develop a complex 3D beam FE model to successfully analyse the static structural response of a concrete cable-stayed bridge equipped with a permanent monitoring system, under the effects of temperature variations. Several authors perform the validation of the dynamic models of railway bridges under traffic loads using only the extreme values of the acceleration records [18, 19]. However, recent studies have demonstrated the importance of taking into account the complete time-history of the accelerations [20] and the corresponding response in the frequency domain [21] in order to improve the accuracy of the validation process. With regard to the validation of the numerical model based on modal information, the literature shows the importance of considering both global and local modal parameters. Matsuoka et al. [21] and Somaschini et al. [22] concluded that high precision estimates of the maximum acceleration of the deck require the inclusion of contributions from the local modes of the deck slab, including track vibration modes, along with conventionally considered global vibration modes. The absence of one or several of these modal contributions could lead to an underestimation of the maximum acceleration values achieved by the motion of the deck.

Although a significant amount of research has focused on model validation using either dynamic or static measurements separately, the complementary relationship between static and dynamic responses should be taken into account to ensure a comprehensively validated FE model, especially regarding the behaviour of long-span bridges [23]-24]. For instance, Wang et al. [25] showed the importance of performing a two-phase model update and validation approach, based on ambient vibration and static measurements, for the longest bridge in China, the Runyang Suspension Bridge. The authors demonstrated that only the ambient vibration test results were insufficient for comprehensively updating and validating an FE model.

Some authors also pointed out the fact that the experimental validation of FE models depends heavily on the amplitude vibration levels generated by different types of loads. Thus, the structural behaviour resulting from low-amplitude actions, such as temperature and ambient actions, may differ from that resulting from high-amplitude actions, such as traffic loads. This is essentially due to the amplitude-dependent behaviour of the materials, e.g., the ballast [26 - [28], and the properties of the material, e.g., the elasticity of the concrete [29], and also the non-linear behaviour of the support bearings and structural joints [30, 6]. Malveiro et al. [31],32] showed that the numerical model of a railway bridge, previously calibrated based on experimental modal parameters, did not adequately reflect the mobility of the bearings due to their non-linear behaviour, which differed if solicited by environmental or traffic actions.

This research work aims at using a structural health monitoring system for the progressive validation of complex non-linear FE models of railway bridges based on static, modal, and dynamic responses. This progressively stepped validation will increase the reliability of numerical models, envisaging further uses, such as condition assessment, simulations under extreme loading scenarios, evaluation of safety and serviceability, and risk analysis. Such capabilities ultimately begin to realize the concept of a “digital twin” for the structure. Additionally, this paper presents an integrated approach that uses SHM measurements in combination with FE modelling to understand the structural behaviour of a long-span bridge. It is shown that dynamic traffic-based SHM system will provide greater sensitivity in detecting the non-linear behaviour of the components of the bridge, possibly related to structural changes, due to the effects of high amplitude actions induced by regular train loading schemes (axle configuration and loads).

After the introduction, sections 2 and 3, respectively, show the case study and the installed Structural Health Monitoring system. Section 4 describes the numerical model and explains the details of the non-linear analyses. Afterwards, in section 5, the validation of the numerical model is presented with the simulation of the responses to ambient vibration, environmental actions and traffic loads, considering abnormal restrains observed in the bearing devices of the bridge. Finally, section 6 lists the main conclusions obtained from the present work, along with the main achievements.

2. Railway bridge over the Sado River

The composite bowstring-arch bridge over the Sado River is located on the railway line that connects Lisbon and the Algarve region, in the South of Portugal (Figure 1a). This bridge is part of a 28.98 km long railway stretch called the Alcácer bypass, located between the Pinheiro Station and km 94 of the above-mentioned Lisbon-Algarve line (Figure 1b). The structure started to be built in November of 2008 and has entered in operation in August of 2010. The bridge is prepared for conventional and tilting passenger trains with speeds up to 250 km/h, as well as for freight trains with a maximum axle load of 25 t. Even though the bridge accommodates two rail tracks, only the upstream track is currently in operation.

The bridge has a total length of 480 m, divided into 3 continuous spans, each with 160 m, and is part of a longer structure that includes the North access viaduct, 1115 m long, and the South access viaduct, 1140 m long.

As shown in Figure 2, the bridge deck is suspended by three arches connected to each span of the deck by 18 hangers distributed over a single plane on the axis of the structure. The hangers have a circular cross-section with a 200 mm diameter and a spacing of 8 m in the longitudinal direction. The superstructure is composed of a steel-concrete composite deck, while the substructure, which includes the piers, the abutments and the pile foundations,

is built in reinforced concrete. As illustrated in Figure 2, the deck is fixed on pier P1, whereas on piers P2, P3 and P4 only the transverse movements of the deck are restrained, while the longitudinal movements are constrained by seismic dampers. The ballasted railway track has an Iberian gauge (1.668 m) composed of continuously welded rails (type UIC60E1) resting on mono-block concrete sleepers.



Figure 1. Alcácer bypass: a) overview of the Sado Bridge, b) geographical location of the bypass and schematic representation adapted from REFER [33].

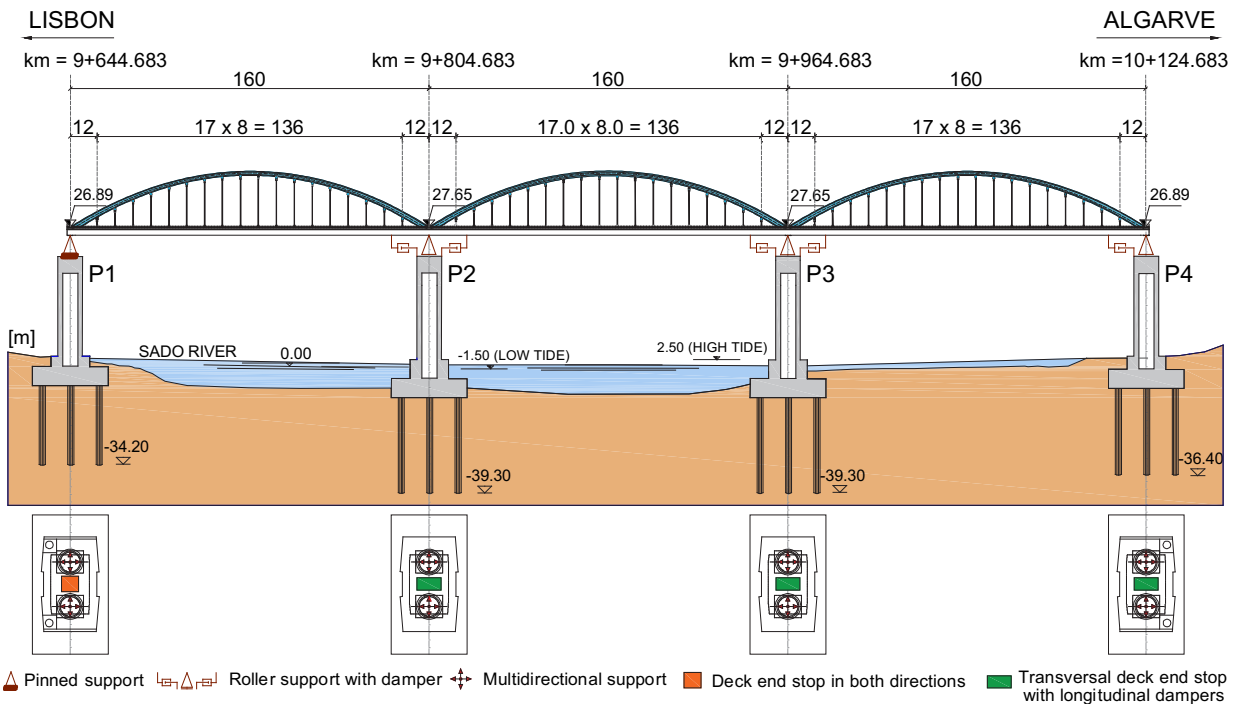


Figure 2. Lateral view of the bridge detailing the bearing devices (adapted from GRID et al. [34]).

The bridge deck consists of a concrete slab laid over a steel box girder. The concrete slab has a total width of 15.85 m and a cross-section thickness ranging from 200 mm at the edge to 430 mm at the bridge’s symmetry plane. The u-shaped steel box girder has a total height of 2.6 m and two inclined lateral webs, a 6.20 m wide bottom flange and three top flanges – two outer ones connected to the lateral webs and one in the middle connected to the cross-section diagonals and hangers (Figure 3a). The top outer flanges are 1.50 m wide, the middle one is 1.20 m, and their thickness varies between 30 mm and 60 mm. The inclined webs are 30 mm thick across the entire length of the deck.

The three parabolic arches have a hexagonal hollow cross-section, with a variable width that increases towards the top. The connection between the deck and the hanger is performed through spherical hinges that allow the

torsional rotation of the deck and prevent fatigue phenomena. The suspension of the deck loads is carried out through the hangers by means of steel diaphragms and two diagonal strings in each connection (Figure 3a).

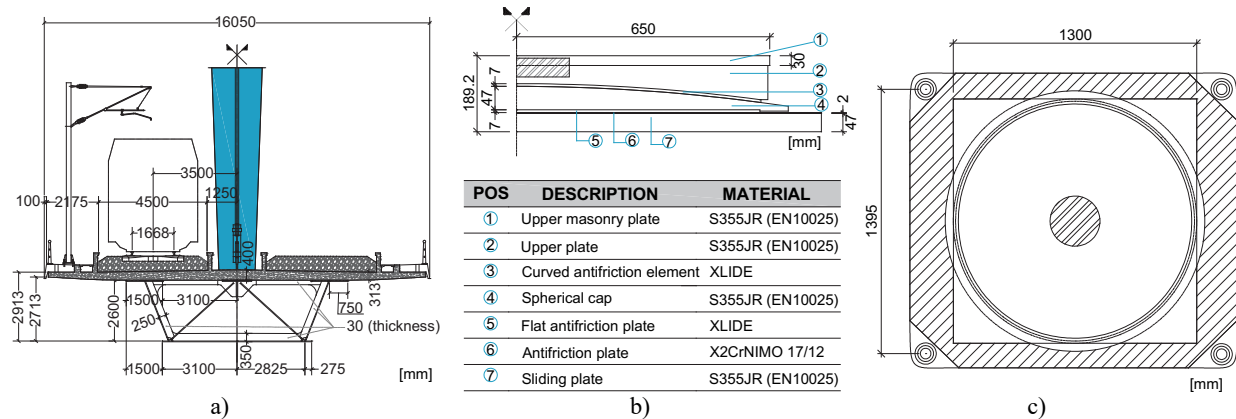


Figure 3. Design drawings: a) Cross-section of the deck, b) half of the bearing lateral view on piers P2/P3, c) floor plan of the bearing on piers P2/P3 (adapted from GRID et al. [34]).

The bridge deck is supported by four reinforced concrete piers with a hollow hexagonal cross-section. Each pier rests on heads of reinforced concrete piles with lengths up to 50 m. Pier heads P1 and P4 are formed by nine piles, while pier heads P2 and P3 are constituted by twelve piles. At the top of each pier, there are two steel spherical multidirectional sliding bearings, 4 m apart. The bearings comprise a circular contact surface, with a 910 mm diameter on piers P1 and P4, and a 1300 mm diameter on piers P2 and P3, and include an antifriction layer in XLIDE material. Figure 3 shows the design drawings of the bearings on piers P2 and P3, as well as the description of the components and materials of each layer.

3. Structural health monitoring system

Immediately after construction, the modal properties of the bridge, namely its natural frequencies, mode shapes and damping coefficients, were assessed through an Ambient Vibration Test (AVT). In addition, the structural health condition of the railway bridge over the Sado River was controlled by periodic visual inspections and using a comprehensive structural monitoring system defined with the objective of controlling the global stiffness of the bridge, the global longitudinal internal forces, as well as the behaviour of its special devices, namely the anti-seismic dampers, the bearings and the joints, to the important actions of temperature and railway traffic. Given this is a single-plane bowstring-arch structure, the important torsional effect due train loading in only one side of the girder, was also taken into account, insofar as the sensors were eccentrically positioned in order to monitor not only effects due to bending but also torsion of the structure. Between November 2011 and November 2016, the system performed static measurements of strain, temperature, and displacement every hour. In November 2016, due to structural changes found in the bearings by visual inspections, an upgrade of the monitoring system was implemented for a better characterization of the behaviour of these devices and the dynamic response of the bridge. This upgrade consisted of additional dynamic measurements performed with accelerometers and displacement transducers located on the top of each pier and in the mid-span deck, so as to take advantage of the excitation induced by the several trains that cross the bridge every day.

The following subsections describe the different phases of the structural health monitoring of the bridge, including the system's architecture, the sensors' network and the analysis of data acquired over the years.

3.1 Architecture

The architecture of the monitoring system followed the aim of a real-time SHM with permanent availability of data. As shown in Figure 4, the acquisition and management system of the Sado bridge is highly distributed, being located in four distinct hardware components. First, the signals from the transducers are acquired through local data acquisition units which then transfer the data to an industrial computer located on the bridge. In turn, this component sends the data to the data management server using a VPN (Virtual Private Network) protocol. Once the data is stored on the database server, it can be accessed by the users.

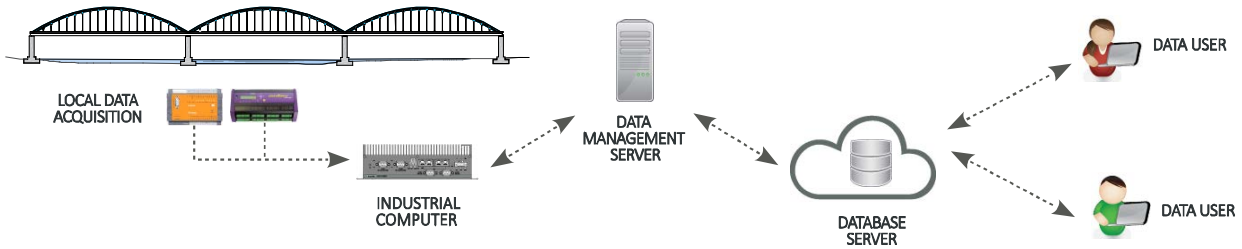


Figure 4. Architecture of the SHM system.

3.2 Ambient vibration test

The Ambient Vibration Test (AVT) covered 25 sections of the deck and 12 sections of the arches, as indicated in Figure 5. The measurements were performed by means of a technique that considers the use of fixed references and mobile measuring points, with a total of 15 uniaxial EpiSensor (ES-U) force balance accelerometers, from Kinemetrics. The ambient vibration response was evaluated in successive setups, measuring: i) vertical accelerations on the downstream side of the slab; ii) vertical and transverse accelerations on the upstream side of the slab; iii) longitudinal accelerations at locations 2, 3, 17, 18, 32 and 33; iv) vertical and transverse accelerations in the arches, and v) vertical and longitudinal accelerations over the bearings. The ambient vibration data was continuously acquired at 500 Hz for approximately 30 minutes during each setup. The measurements were made with a precision $\pm 2 \mu\text{g}$.

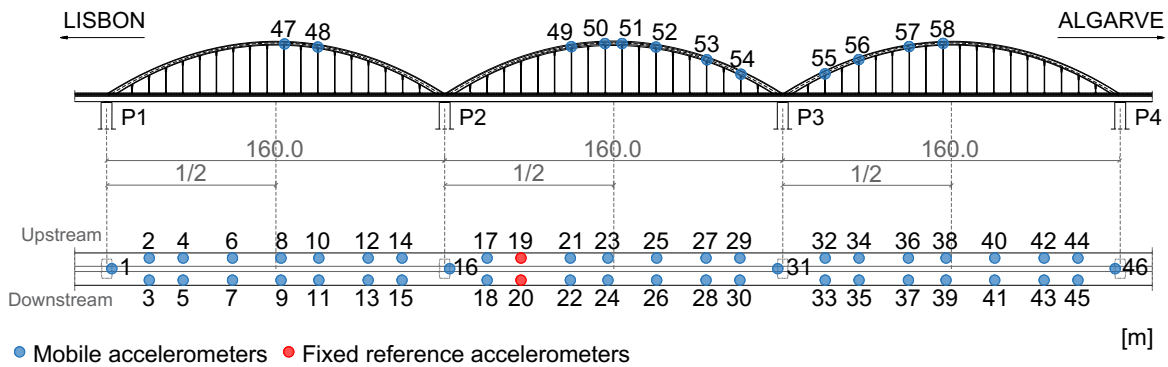


Figure 5. Measuring points of the ambient vibration test.

The AVT allowed the identification of the modal properties of the bridge to establish a baseline condition, comprising 22 vibration modes, characterized by their frequencies, mode shapes and damping coefficients. This identification was performed by applying the Enhanced Frequency Domain Decomposition method (EFDD), available in the ARTeMIS software [35]. Figure 6 shows the curves of the average normalized singular values of the spectral density matrices. Five lateral modes of the arches are outlined on the first curve (Figure 6a), as well as sixteen vertical vibration modes associated with the deck and arches on the second curve (Figure 6b), and one

longitudinal mode of the deck on the third curve (Figure 6c). The first 10 of the 22 mode shapes, frequencies and damping coefficients experimentally identified are plotted in Figure 7.

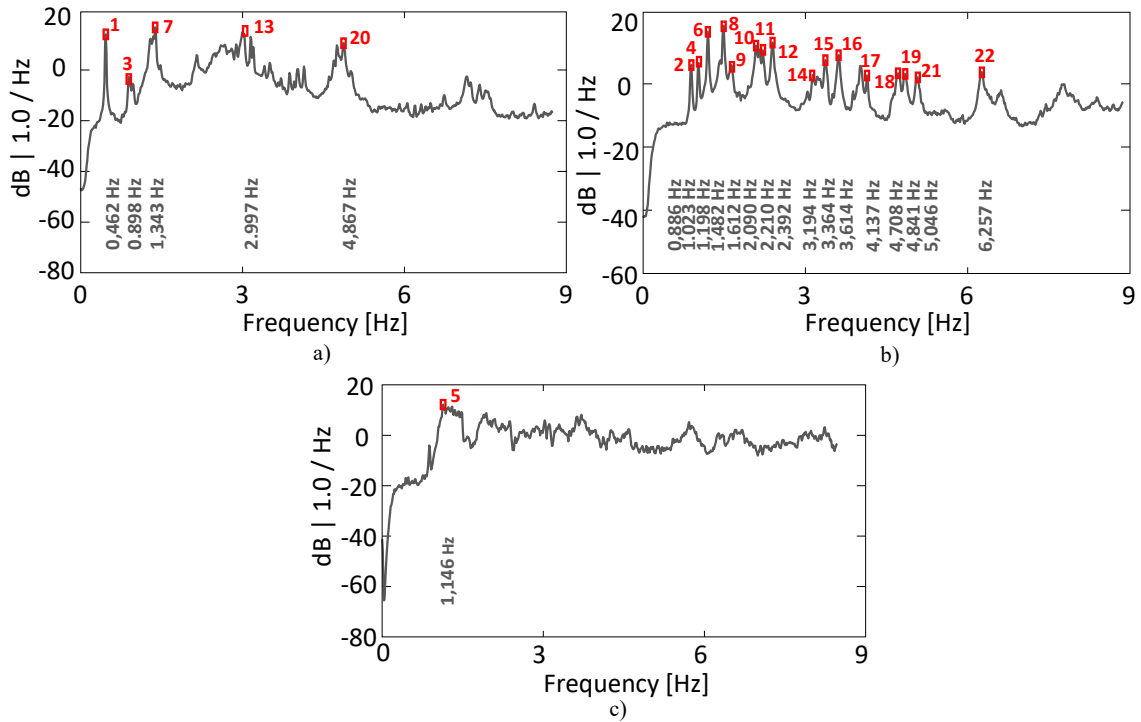


Figure 6. EFDD method: average normalized singular values of the spectral density matrices: a) lateral modes of the arches, b) vertical modes of the deck and the arches, c) longitudinal mode of the deck [36].

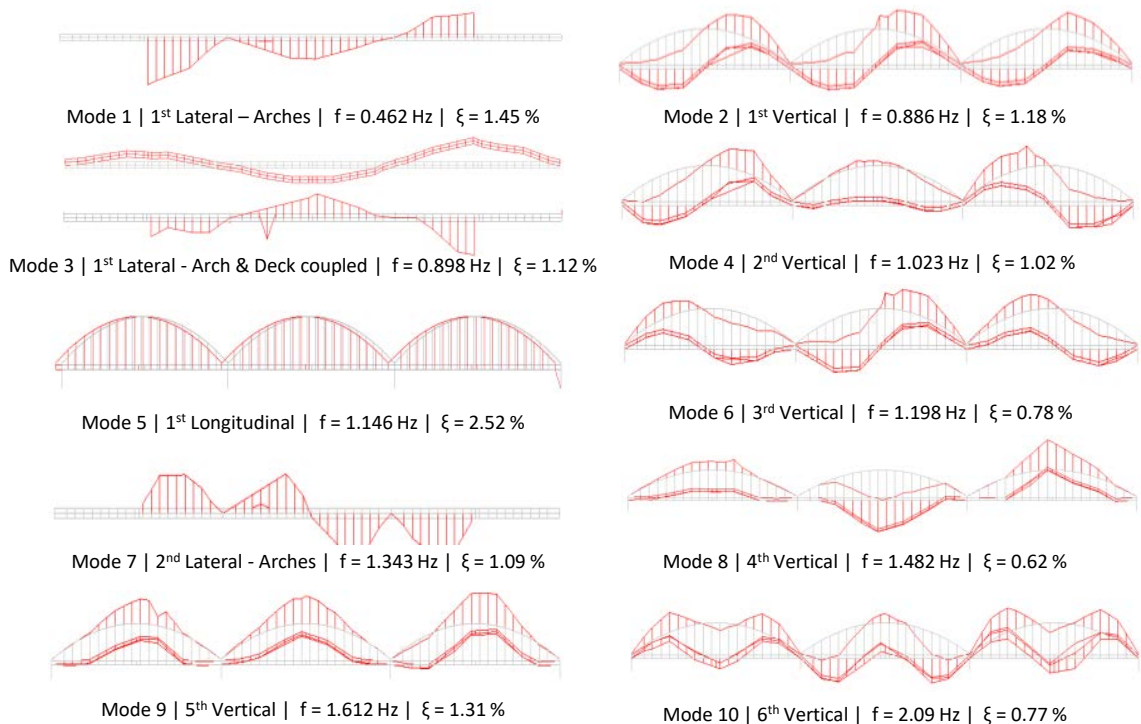


Figure 7. Experimental mode shapes, natural frequencies and damping coefficients [36].

3.3 Static monitoring

As previously mentioned, the first phase of the Sado Bridge monitoring, carried out between November 2011 and November 2016, was mainly concerned with monitoring the stress on the arches and on the deck, as shown in

Figure 8. Figure 9 to Figure 11 show the scheme and details of the instrumented sections. The structural temperature action was measured using NTC thermistors and PT100 sensors. Twelve NTC thermistors were installed in three sections of each arch, as outlined in Figure 9a, b. Additionally, measurements were also taken from four NTC thermistors fixed to the steel box girder and three PT100 sensors embedded in the concrete slab, as illustrated in the cross-section of Figure 10a. Regarding the stress measurements, responses were obtained from the electrical resistance strain gauges installed as a full Wheatstone bridge in the arches (Figure 9c) and fixed to the steel box (Figure 10b,c). To control the increased friction in the bearings, the responses measured by a longitudinal displacement transducer installed at pier P4 (Figure 11) were evaluated.

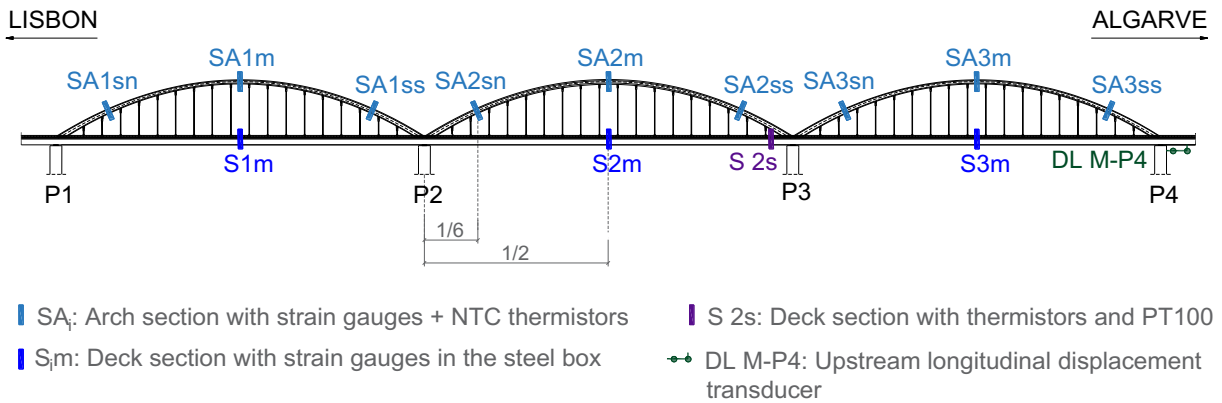


Figure 8. Sensors installed for static measurements.

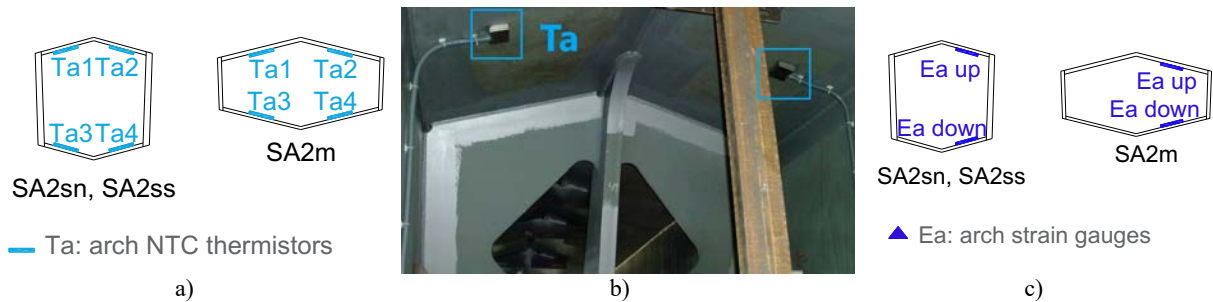


Figure 9. Arch sections: a) NTC thermistors (Ta) location, b) NTC thermistors (Ta) installation, c) strain gauges (Ea) location.

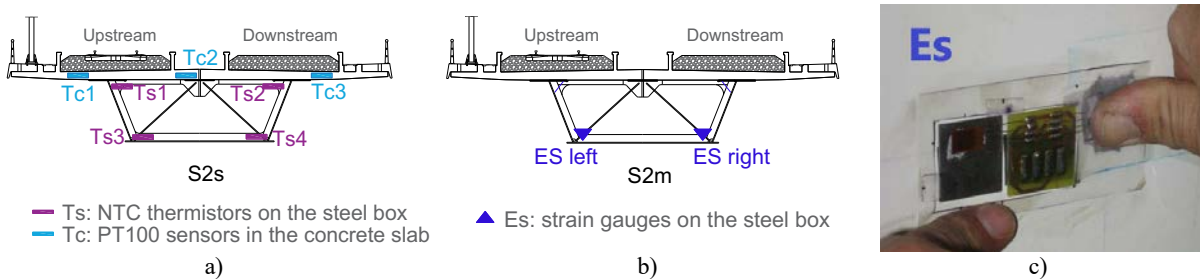


Figure 10. Bridge cross section: NTC thermistors in the steel box (Ts) and PT100 sensors in the concrete slab (Tc), b) strain gauges in the steel box (Es), c) electric strain gauge (Es) installation.



Figure 11. Longitudinal displacement transducer (DL): a) cross section location, b) sensor installation.

Between 2011 and 2016, visual inspections allowed observing, for the bearing devices located on piers P2 and P3, excessive deformations of the spherical cup (Figure 12a), excessive relative displacements between the upper plate and the spherical cup (Figure 12b) and an apparently insufficient thickness of the sliding element (XLIDE) located between the upper plate and the spherical cup (Figure 12c). These findings suggested that the bearings were not fully unrestrained and could result in increased friction between the piers and the deck.



Figure 12. Information obtained from visual inspections carried out on the bearings of piers P2 and P3 of the Sado bridge.

However, as observed in Figure 13, the static-based global monitoring system failed to capture these slight changes in the behaviour of the bridge. This figure shows the evolution of the longitudinal displacements of the bearings on pier P4, the only one comprising dedicated sensors at that time, along with the temperatures measured in the arch (upper fiber – Ta1, and bottom fiber – Ta2), steel box (Ts3) and concrete slab (Tc2), between November 2011 and November 2016. When comparing the two plots, the longitudinal displacement is characterized by a long-period cycle directly related with the annual variation of temperature. The expansion and contraction of the bridge has, therefore, a straight correlation with the seasonal variation of the temperature. Moreover, no deviations or unexpected variations are identified, suggesting that the changes in the bearings of piers P2 and P3 did not influence the overall response of the bridge measured between the deck and pier P4.

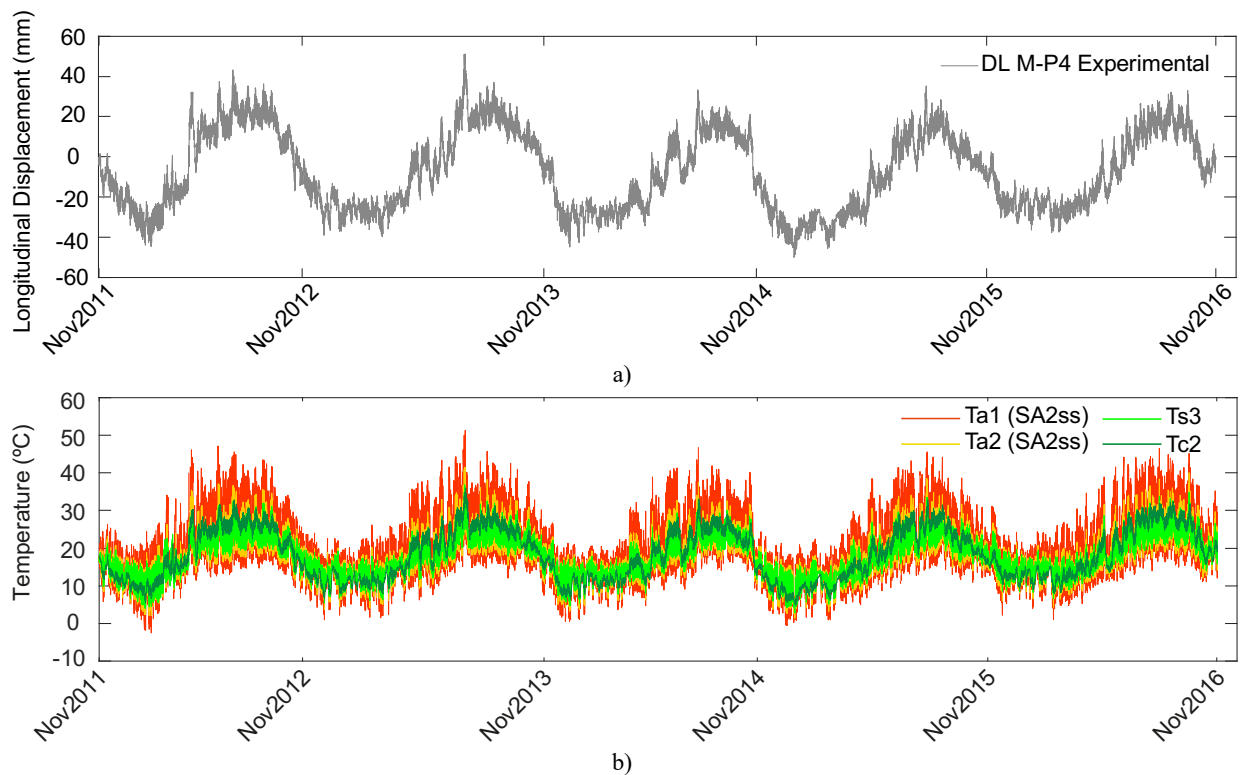


Figure 13. Data acquired between November 2011 and November 2016: a) longitudinal displacements of the upstream bearing located at pier P4 and b) temperature measurements in the middle arch (Ta1 and Ta2), steel box (Ts3) and concrete slab (Tc2).

Although visual inspections suggested changes in the behaviour of the bearing devices, it was not possible to estimate their exact time frame. Therefore, these observations led to the conclusion that more sensors needed to be

installed, specifically in the bearings that presented structural changes, and, above all, that the migration from static to dynamic monitoring is of the utmost importance in order to take advantage of the excitation induced by the several trains that cross the bridge every day.

3.4 Dynamic monitoring

In November 2016, an additional set of transducers was installed on the Sado bridge (Figure 14), mainly for the dynamic measurement of accelerations and displacements. This new set included two pairs of optical sensors, model E3SAT31, at both ends of the bridge, to capture the speed of the trains and carry out the detection of the axle (Figure 15a,b), four longitudinal MEMS DC accelerometers, model PCB 3711E112G, on each pier between the bearings (Figure 15a,c), and two vertical piezoelectric accelerometers, model PCB 393A03, fixed at mid-span of the concrete slab and the steel box girder (Figure 16). The measurements of the longitudinal displacement transducers were acquired from sensors adjacent to each of the eight bearing devices (Figure 11). Unlike the static data acquisition system, which saves measurements every hour, this system acquires the responses of the bridge continuously, in order to save the time history while the train is crossing the bridge, at a sampling rate of 2000 Hz.

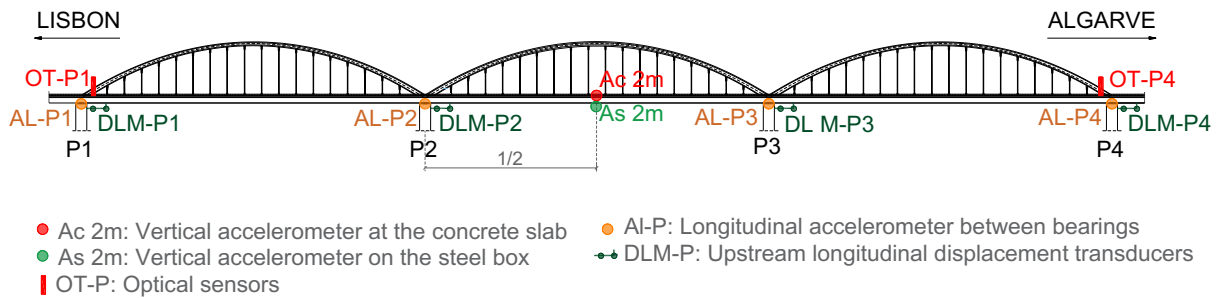


Figure 14. Measurement system: optical sensors, accelerometers and displacement transducers.

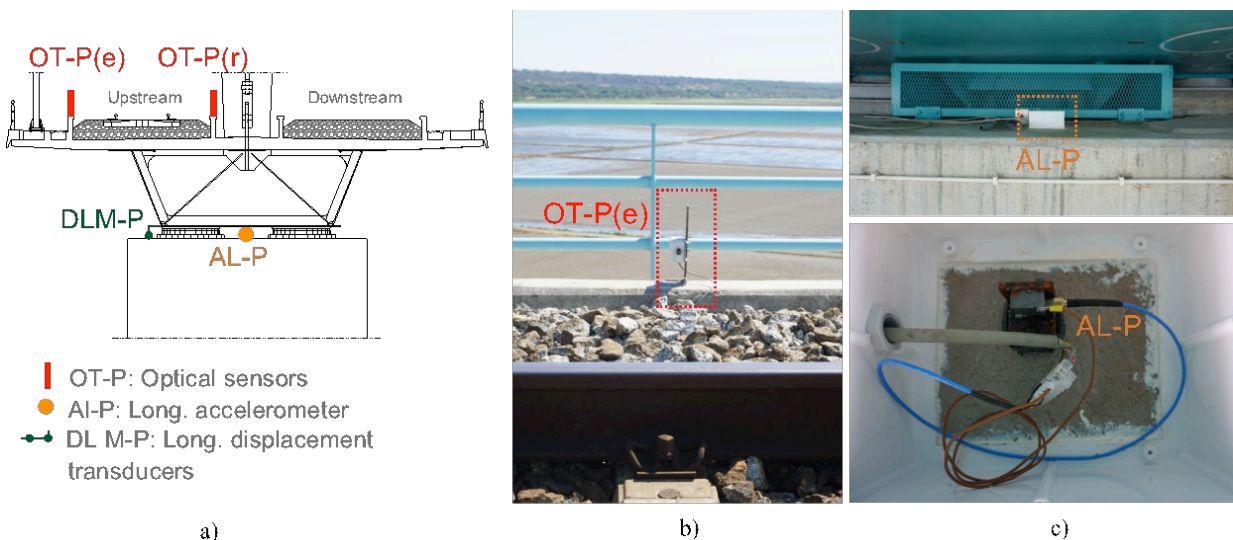


Figure 15. Sensors installed in the section aligned with pier P4: a) cross section of the bridge, b) optical sensor (OT-P), c) longitudinal accelerometer located between bearings (AL-P).

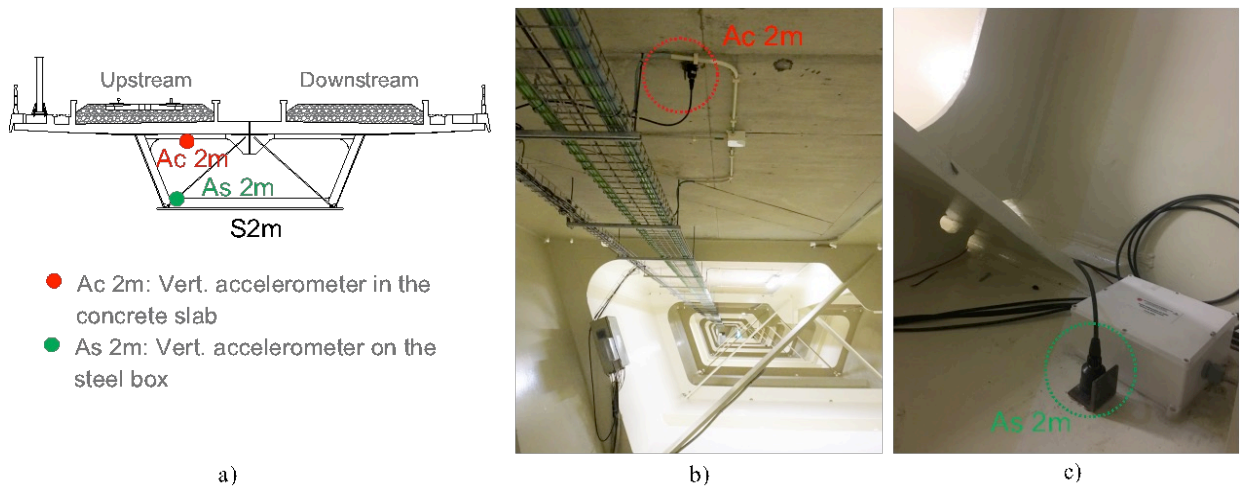


Figure 16. Accelerometers installed at the second mid-span: a) cross section of the bridge, b) vertical accelerometer fixed to the concrete slab (Ac 2m), c) vertical accelerometer fixed to the steel box (As 2m).

In order to evaluate the evolution of the friction coefficient of the bearings, an analysis of the data acquired continuously on piers P2, P3 and P4 was conducted using longitudinal accelerometers and longitudinal displacement transducers.

Figure 17a. presents the analysis of the behaviour of the bearings on each pier for a period of 24 hours. The bearing response depends on the combined action of a vertical load (FN) and a horizontal load (FH). For a friction coefficient μ , the bearing will slide if the criteria of yielding ($FH = \mu|FN|$) is verified. The sliding of the bearing varies depending on the temperature and the train-induced vibration applied at a specific instant. The longitudinal accelerations shown in this figure allow observing that 17 trains crossed the Sado Bridge on December 2, 2016. The amplitude of these responses varies, depending on the type of train. Furthermore, the responses measured by the accelerometer on pier P4 display higher amplitudes, when compared with the ones on piers P2 and P3. A direct correspondence can also be observed between the acceleration measurements for each train that crossed the bridge and the displacement of the upstream bearing on pier P4, highlighted by dashed lines. During the observation period shown in Figure 17a, the bearing on pier P4 slides in one direction in the morning, in the opposite direction in the afternoon, and changes direction again during the night. This behaviour is clearly influenced by the variation of the structure's temperature throughout the day. Due to the sun exposure of the bridge, the upper fibre of the arch (Ta1) presents the greatest temperature variation. On the other hand, the transducers located on the bearings of piers P2 and P3 recorded near-null longitudinal displacements during the passage of all trains.

Each plot of Figure 17a comprises a dashed window highlighting the responses acquired between 9 and 10 am, shown in Figure 17b. Over the course of this one-hour window, all longitudinal accelerometers recorded amplified responses during the passage of 2 trains. The upstream bearing on pier P4 systematically slides when a train is passing, always in the same direction but with different amplitudes. It is not possible to observe the influence of temperature on the behaviour of the bearing here, but it is easier to identify the bearing displacement caused by a passing train. However, the bearings on piers P2 and P3 show near-null values during the passage of the same trains, which corroborates the conclusions obtained in the visual inspections. In addition, it can be observed that during this hour the temperatures in the steel box (Ts3), in the concrete slab (Tc2) and in the middle arch (Ta1-upper fibre and Ta2 - bottom fibre) are practically stable.

This analysis allowed observing the combined actions of temperature and train-induced vibration in the bearing devices. It is possible to conclude that the static deformation imposed to the bearing devices by the temperature is much more preponderant than the dynamic longitudinal displacement inflicted by a train crossing. The degradation of

the friction coefficient changes the bearing behaviour, which can lead to the full restraints of its movements, as verified in piers P2 and P3. It was confirmed that a dynamic monitoring system has the advantage of detecting bearing defects based on the excitation induced by passing trains. With the passage of several trains, the diagnosis can be validated, and false positives can be dismissed in a short period of time.

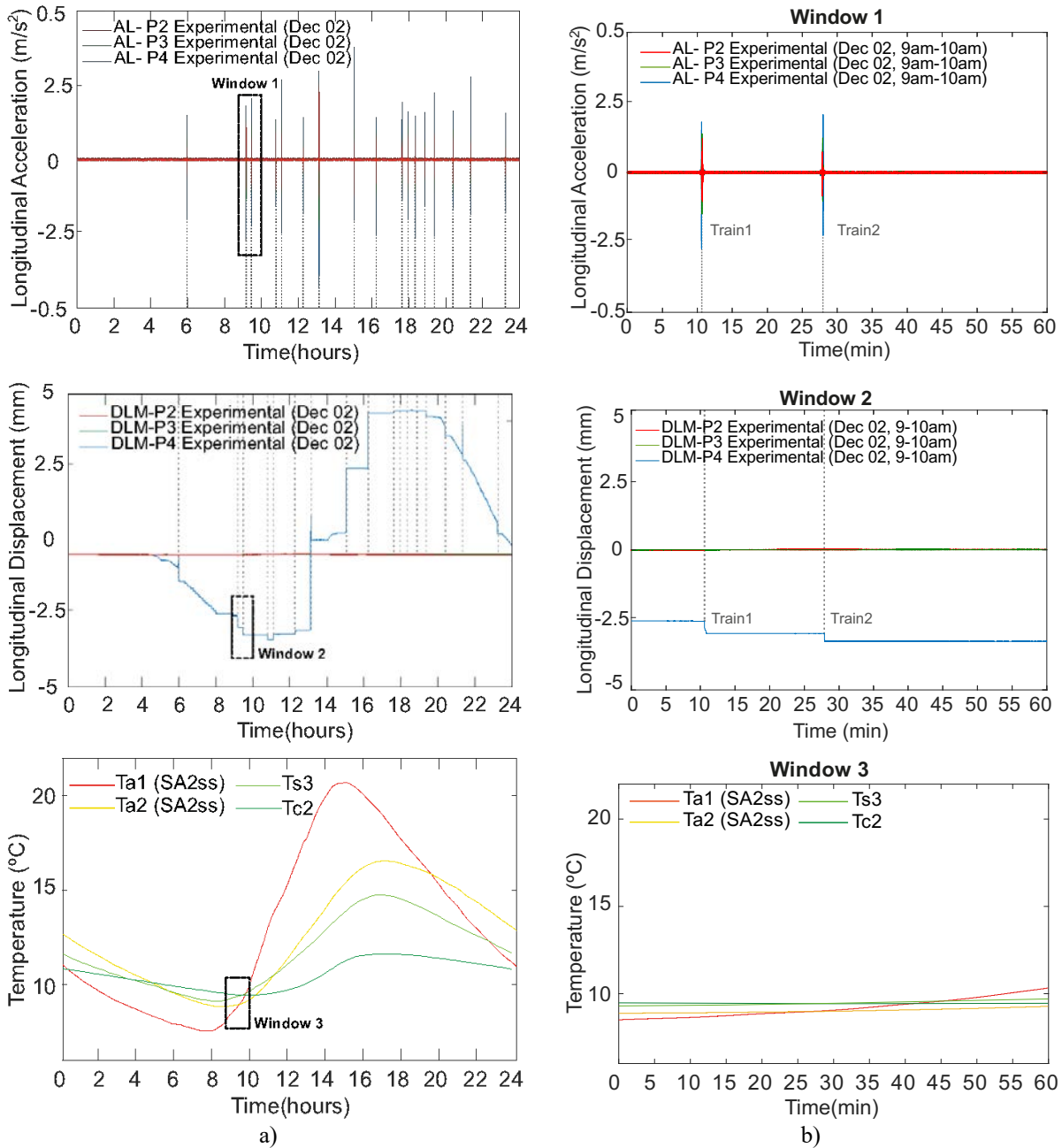


Figure 17. Analysis of the longitudinal accelerations and displacements on piers P2, P3 and P4, and the temperature of the structure measured on December 2, 2016: a) for 24 hours and b) for 1 hour.

4. Numerical modelling

4.1 Description

A 3D finite element numerical model of the bridge was developed in the ANSYS [37] software. The deck, hangers and arches were previously modelled by Albuquerque et al. [38]. The assessment of the structural changes

discussed in section 3 led to the need to develop a numerical model that accurately simulates the longitudinal response of the bridge and the non-linear behaviour of the bearings. For that purpose, the upgraded numerical model developed in the present study also includes the track, the bearings, the piers and the foundations, as shown in Figure 18.

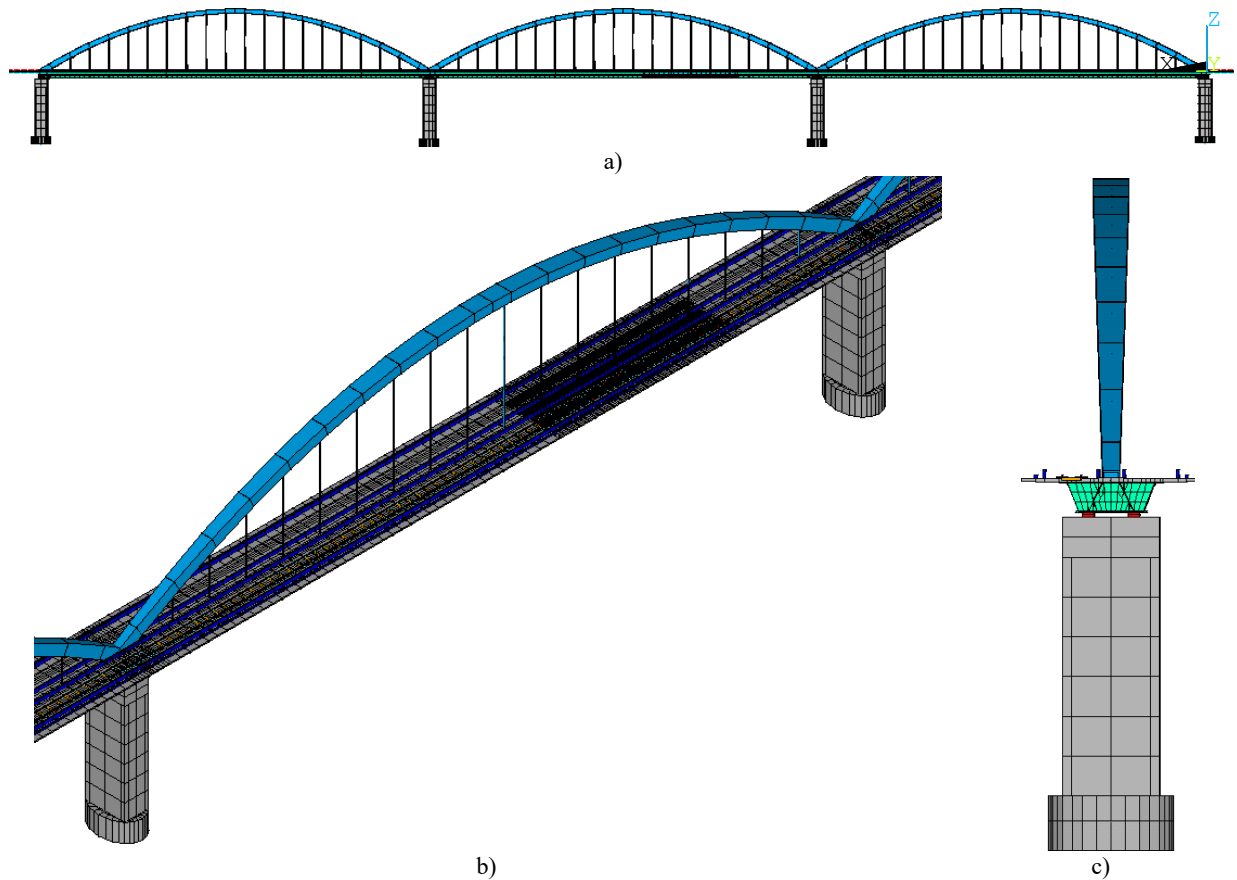


Figure 18. 3D numerical model of the railway bridge over the Sado river: a) lateral view, b) middle span detail, c) front view.

Among the modelled structural elements, those defined as beam finite elements consist of piers, sleepers, ballast-containing beams, rails, arches, hangers, transverse stiffeners, diaphragms and diagonals. Shell elements were used to model the concrete slab and the steel box girder, while the pads, the ballast layer and the foundations were modelled using linear spring-dashpot assemblies. The mass of the non-structural elements and the ballast layer was distributed along the concrete slab. Concentrated mass elements were used to reproduce the mass of the arches' diaphragms and the mass of the sleepers, which were simply positioned at their extremities. The connection between the concrete slab and the upper flanges of the steel box girder, as well as the connection between the deck and the track, were performed using rigid links. Special attention was paid to the bearings supports, as they can strongly influence the performance of the bridge. Hence, in order to simulate the sliding behaviour of the bearings, non-linear contact elements were applied. Moreover, constraint elements located between the bearings were used to restrict the transversal movement in each pier, and the longitudinal and transversal movements in the case of the first pier. It is worth mentioning that the seismic dampers were not modelled, as they are not activated during serviceability loads, such as the ones caused by passing trains or environmental actions. Figure 19 illustrates a schematic representation of the numerical model highlighting the different types of finite elements that were used.

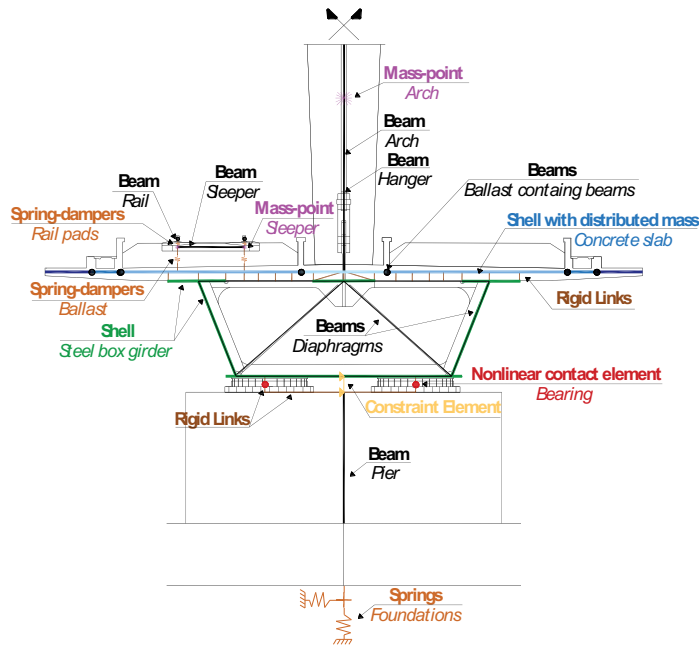


Figure 19. Schematic cross-section representation of the FE numerical model.

A mesh of elements with a discretization of less than 2 m in the longitudinal direction was adopted for most of the deck. However, a more refined mesh was defined at the central third of the second span for a more precise characterization of the dynamic responses under traffic loads (Figure 20b). To ensure a correct representation of the transition zones between the structure and the embankment, an extension of the track and sleepers, spaced 0.6 m, was modelled at both ends of the bridge (Figure 20a). The numerical model of the bridge includes 25924 nodes and 38620 finite elements.

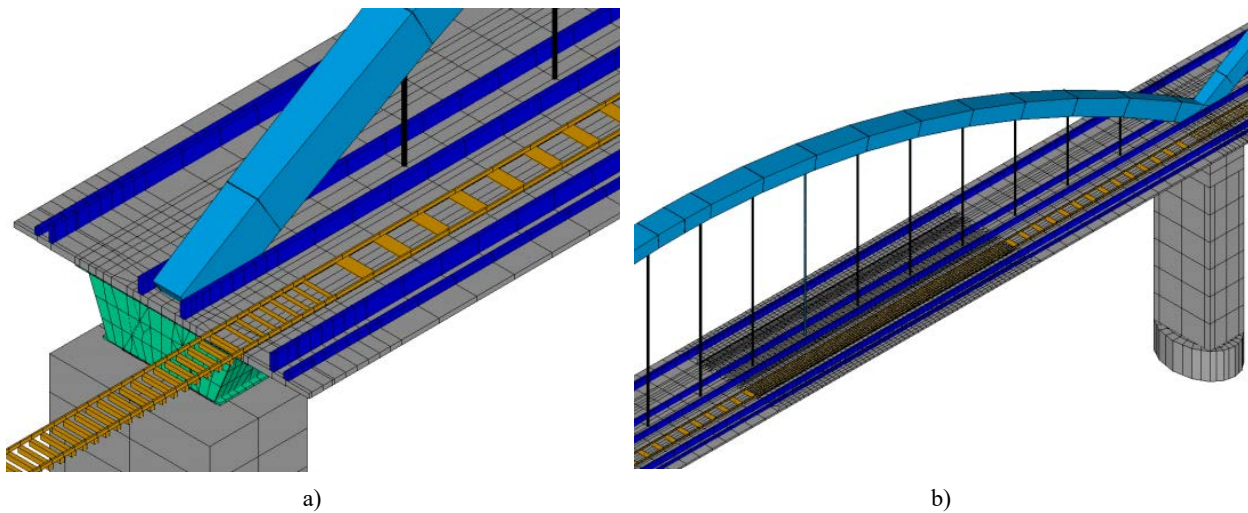


Figure 20. Details of the numerical model: a) transition zone, b) refined mesh in the second span.

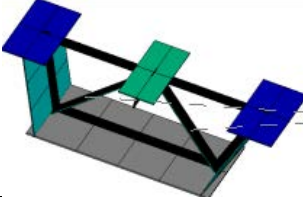

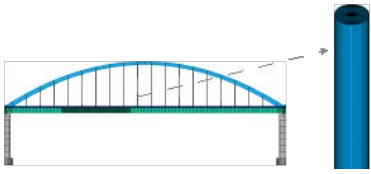
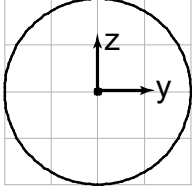
4.2 Geometrical and mechanical properties

The following subsections present a detailed explanation of the main geometrical and mechanical parameters of the different structural components of the numerical model.

4.2.1 Superstructure

The steel of the deck was defined with a modulus of elasticity of 210 GPa, a Poisson's ratio of 0.3 and a density of 7850 kg/m³, while the concrete slab was defined with a density of 2500 kg/m³, a Poisson's ratio of 0.15 and a modulus of elasticity of 43 GPa, based on the updated model presented by Albuquerque et al. [38]. The diagonal elements located in each diaphragm have the geometrical properties specified in Table 1. The arches were composed of variable cross-sections, with varying thickness, width and height, both of flanges and webs. Their geometric and mechanical characteristics were reproduced in the numerical model along with the nodal masses added to the hanger-to-arch connections, which replicate the diaphragms built in those locations. Regarding the hangers, their cross-sections consist of a circumference with a 200 mm diameter and the properties presented in Table 1. Both the arches and the hangers were modelled in steel with the same characteristics as the one used in the deck box girder.

Table 1. Geometrical parameters of the diagonals of the diaphragms and hangers.

NUMERICAL MODEL DETAIL	CROSS-SECTION	GEOMETRICAL PROPERTIES
		$A = 0.035 \times 0.60 = 0.021 \text{ m}^2$ $I_y = 0.214 \times 10^{-5} \text{ m}^4$ $I_z = 0.630 \times 10^{-3} \text{ m}^4$ $J = 0.828 \times 10^{-5} \text{ m}^4$
		$A = 3.14 \times 10^{-2} \text{ m}^2$ $I_y = 7.85 \times 10^{-5} \text{ m}^4$ $I_z = 7.85 \times 10^{-5} \text{ m}^4$ $J = 1.57 \times 10^{-4} \text{ m}^4$

4.2.2 Bearings

The bearing devices were modelled using non-linear contact elements CONTA178 [37]. These elements allow contact and sliding between any pair of nodes, and are able to withstand compression forces normal to their plane and friction forces along the tangential directions based on the Coulomb model. Their friction coefficient μ was defined as 1.5% during the numerical analysis, based on the specifications of the design [33].

As observed in Figure 21, the force deflection relationships for the contact element were separated in the normal and tangential (sliding) directions. In the normal direction, when the normal force (FN) is negative, the contact status remains closed. In this circumstance, in the tangential direction, if the absolute value of the tangential force (FS) is below $\mu|FN|$, the contact element works as a linear spring; otherwise, if $FS = \mu|FN|$, sliding will occur. As FN becomes positive, the contact is broken and no force is transmitted (FN = 0, FS = 0). This non-linear contact problem is solved by the Penalty method [39].

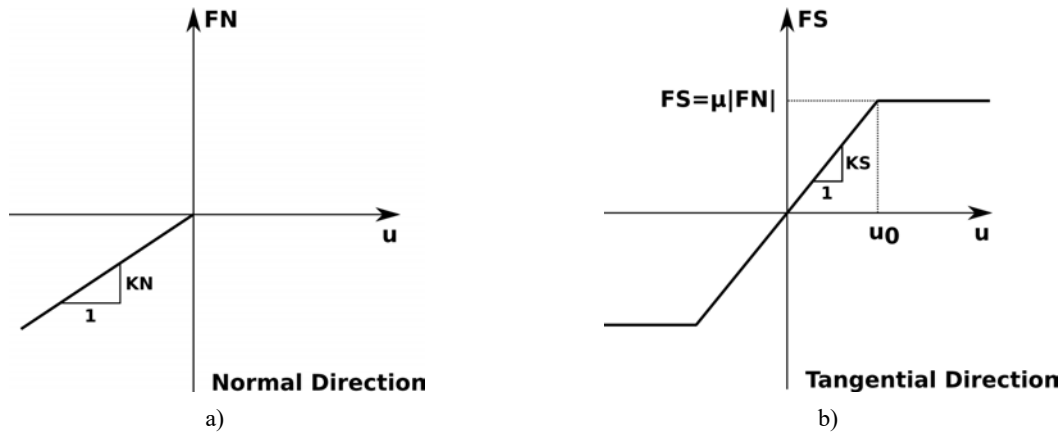


Figure 21. Force-deflection relationship of the contact element: a) normal direction, b) tangential direction.

4.2.3 Substructure

The piers are composed of three different types of reinforced concrete cross-sections, namely, a solid rectangular section, a rectangular hollow-section, and an elliptical hollow-section. The geometric properties of each section are presented in Table 2. The two central piers were modelled with the same height (25.72 m), while the first and fourth are slightly shorter (23.10 m and 23.68 m, respectively). The piers were modelled using a concrete with a density of 2500 kg/m³, a Poisson's ratio of 0.15 and a modulus of elasticity of 43 GPa.

Table 2. Geometrical properties of the piers.

NUMERICAL MODEL DETAIL	CROSS-SECTION	GEOMETRICAL PROPERTIES
		$A = 44.20 \text{ m}^2$ $I_y = 99.60 \text{ m}^4$ $I_z = 266.12 \text{ m}^4$ $J = 250.81 \text{ m}^4$
		$A = 19.36 \text{ m}^2$ $I_y = 72.77 \text{ m}^4$ $I_z = 167.57 \text{ m}^4$ $J = 164.50 \text{ m}^4$
		$A = 42.74 \text{ m}^2$ $I_y = 234.78 \text{ m}^4$ $I_z = 406.44 \text{ m}^4$ $J = 560.07 \text{ m}^4$

The boundary conditions were modelled using the results obtained from *in-situ* geotechnical tests conducted during the construction of the bridge [33]. The Standard Penetration Test (SPT) was done twice on each pier, while the Crosshole Test was specifically conducted on pier P3.

The flowchart presented in Figure 22 illustrates the several steps taken to obtain an equivalent soil stiffness in each direction, which was later included in the numerical model of the bridge using spring elements. During these calculations, the *N-values* of the SPT and the shear wave velocity of the soil (V_s), obtained from the *in-situ* tests, were considered, together with the classification of the soil resulting from the laboratory analyses of the samples

collected during the same tests. The equivalent soil stiffness (k_{trans} and k_{rot}) computed on each pier is indicated in Table 3.

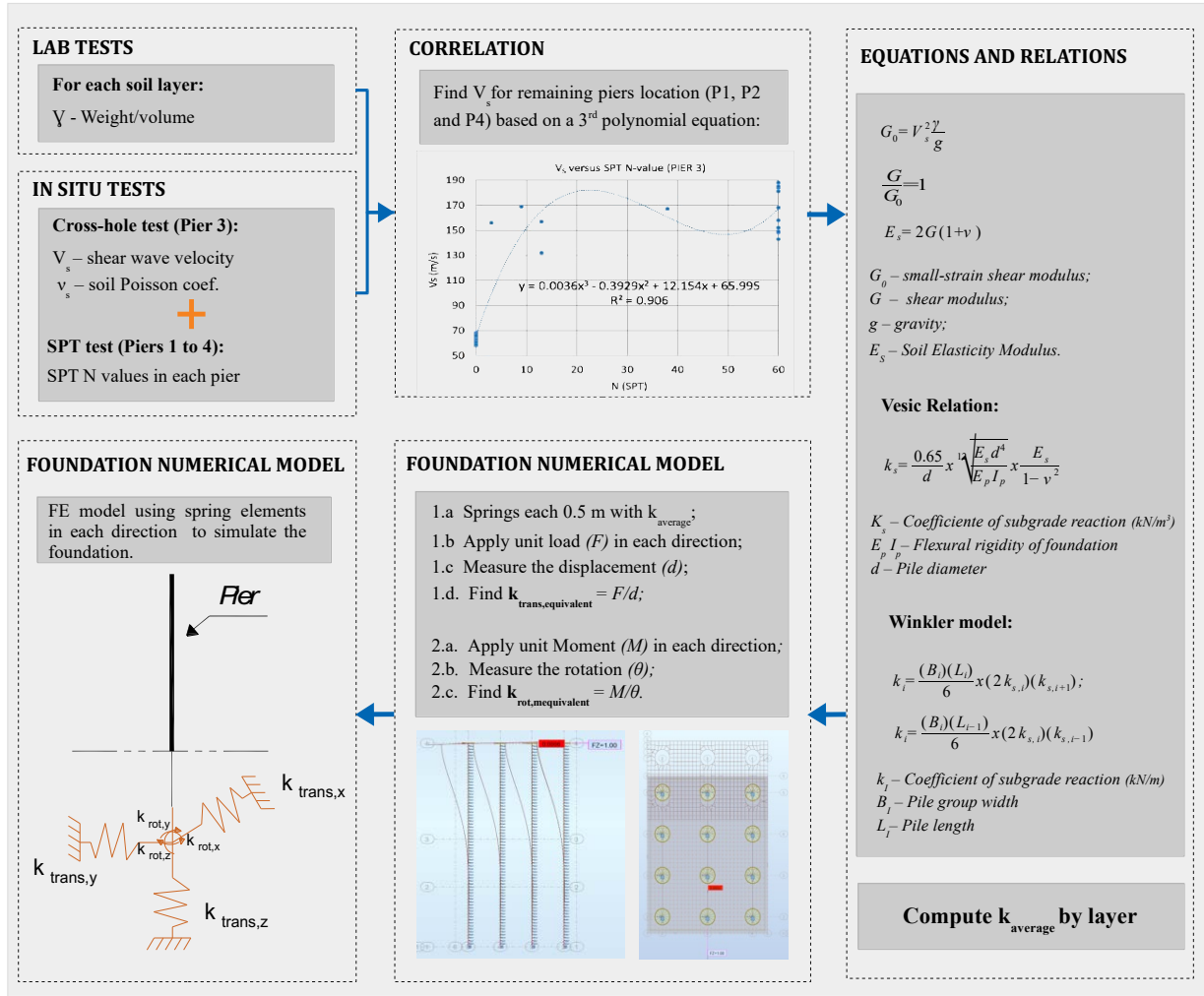


Figure 22. Flowchart describing the simulation of the soil stiffness.

Table 3. Equivalent soil stiffness considered on each pier.

PARAMETER	P1	P2	P3	P4	UNITS
$k_{trans,x}$	1.11E+06	1.43E+06	1.25E+06	1.00E+06	kN/m
$k_{trans,y}$	1.11E+06	1.67E+06	1.25E+06	1.00E+06	kN/m
$k_{trans,z}$	1.00E+12	1.00E+12	1.00E+12	1.00E+12	kN/m
$k_{rot,x}$	1.33E+09	2.09E+09	2.09E+09	1.19E+09	kN/m
$k_{rot,y}$	1.33E+09	1.61E+09	1.61E+09	1.19E+09	kN/m
$k_{rot,z}$	1.93E+09	3.70E+09	3.70E+09	1.72E+09	kN/m

4.2.4 Railway track

The geometric and mechanical properties of the UIC60 rail were adopted following the guidelines of the EN 13674-1 [40] and UIC 861-3 [41] standards. The modulus of elasticity, density weight and Poisson's ratio of the steel were considered equal to 210 GPa, 7850 kg/m³ and 0.30, respectively. The main properties of the track, such as the stiffness and damping of the ballast and rail pads, were adopted from the literature or from previous research work and summarized in Table 4. It is worth pointing out that the ballast mass was distributed over the slab and that the

inertia and geometry of these elements were corrected to take into account the different mesh discretization adopted along the deck.

Table 4. Mechanical properties of the numerical model of the track.

	DESIGNATION	PARAMETER	VALUE	UNITS	REFERENCE
Ballast	Longitudinal stiffness	$K_{bal,l}$	30	MN/m/m	UIC 774-3-R [42]
	Transversal stiffness	$K_{bal,t}$	7.5	MN/m/m	ERRI D 202/RP 11 [43]
	Vertical stiffness	$K_{bal,v}$	100	MN/m/m	
	Damping (3 directions)	C_{bal}	50	kN.s/m/m	Wu & Yang [44]
Rail pads	Longitudinal stiffness	$K_{fas,l}$	20	MN/m	Zhai et al. [45]
	Transversal stiffness	$K_{fas,t}$	20	MN/m	Paixão et al. [46]
	Vertical stiffness	$K_{fas,v}$	160	MN/m	
	Rotational stiffness	$K_{fas,r}$	45	kN.m/rad	ERRI D 202/RP 11 [43]
	Longitudinal damping	$C_{fas,l}$	50	kN.s/m	Zhai et al. [45]
	Transversal damping	$C_{fas,t}$	50	kN.s/m	
	Vertical damping	$C_{fas,v}$	17	kN.s/m	Paixão et al. [46]
Concrete sleeper	Modulus of elasticity	$E_{c,sleeper}$	30	GPa	Paixão et al. [46]
	Poisson's ratio	$\nu_{c,sleeper}$	0.25	-	

4.3 Non-linear numerical analyses

4.3.1 Static analysis

The structural static behaviour of the bridge was simulated in the FE model by running a time-history analysis using experimental data as input. The simulation procedure consisted of using the temperatures acquired every hour on site over the course of one year, some of which are shown in Figure 23, as input for the numerical simulations, and obtaining the corresponding output, composed of time-series of displacements and deformations. Each time series used in the numerical simulation consists of over 8400 data points, spanning over a period of 12 months (between November 2015 and November 2016). Figure 23 also shows a lateral view and a section detail of the numerical model, including the experimental temperatures from one hour of a day in November.

A clustering strategy was considered regarding the input of the experimentally acquired temperatures. As it is possible to observe, the steel box was divided into four clusters (Ts1, Ts2, Ts3 and Ts4), the concrete slab was divided into three (Tc1, Tc2 and Tc3), and each arch was also divided into three clusters (SA2sn, SA2m and SA2ss), with the temperature being introduced in the upper (Ta1) and bottom (Ta2) part of the arch section. A reference temperature of 30° C was considered in the simulations, according to the average seasonal temperature at the time the bridge was completed.

To ensure that the numerical model accurately described the structural behaviour of the bridge during the numerical analysis, the non-linear contact elements simulating the bearings were activated. The Full Newton-Raphson Method implemented in the ANSYS software was used to solve the non-linear problem.

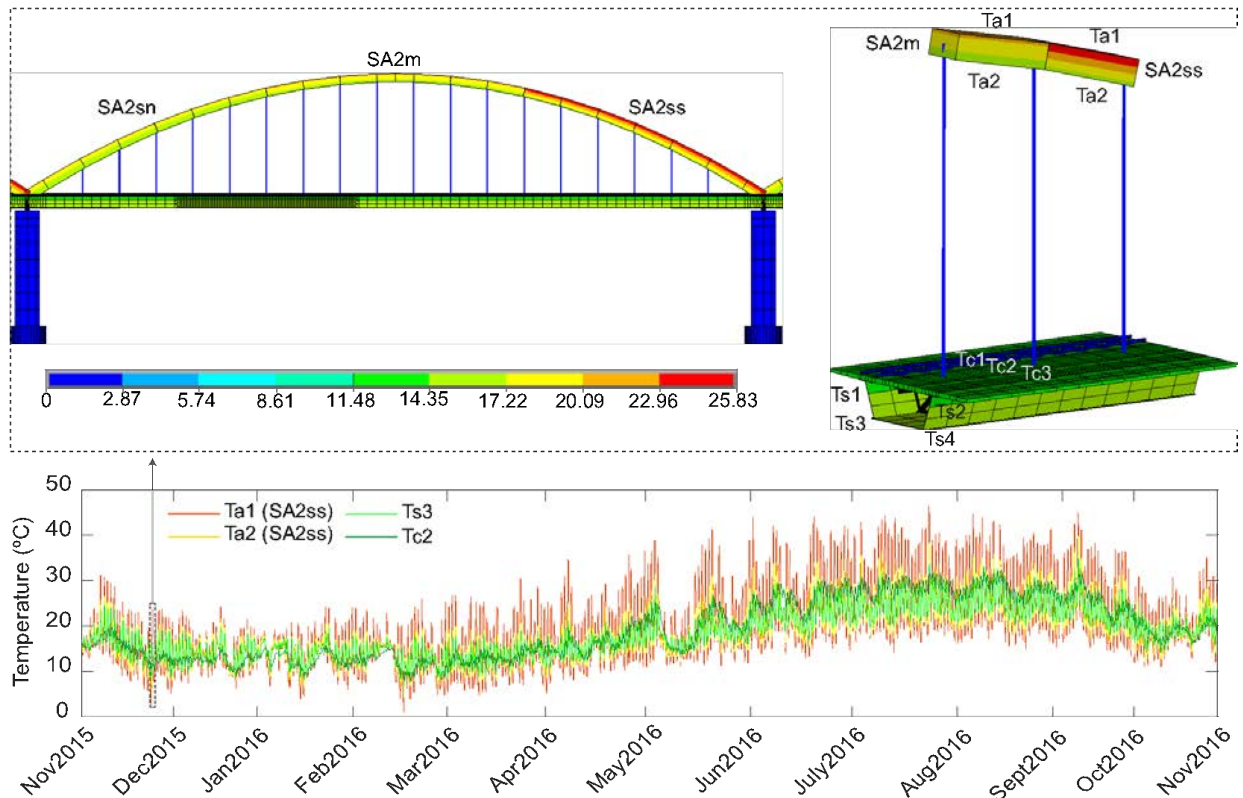


Figure 23. Experimental temperatures used as input for the numerical time history simulation.

4.3.2 Dynamic analysis

Dynamic numerical simulations were conducted in order to reproduce the structural quantities that were measured in the exact locations of the real sensors, installed on site. To faithfully reproduce these structural responses, the action of the measured temperature (from the sensors mentioned in section 3) precisely during the passage of each train is introduced as input in the numerical model.

Using the measurements of the optical sensors setup installed at both ends of the bridge, it is possible to compute the speed of the train and identify the type of train, according to its geometry. Figure 24 shows an example of the optical sensors' response when an Alfa Pendular train crosses the Sado bridge.

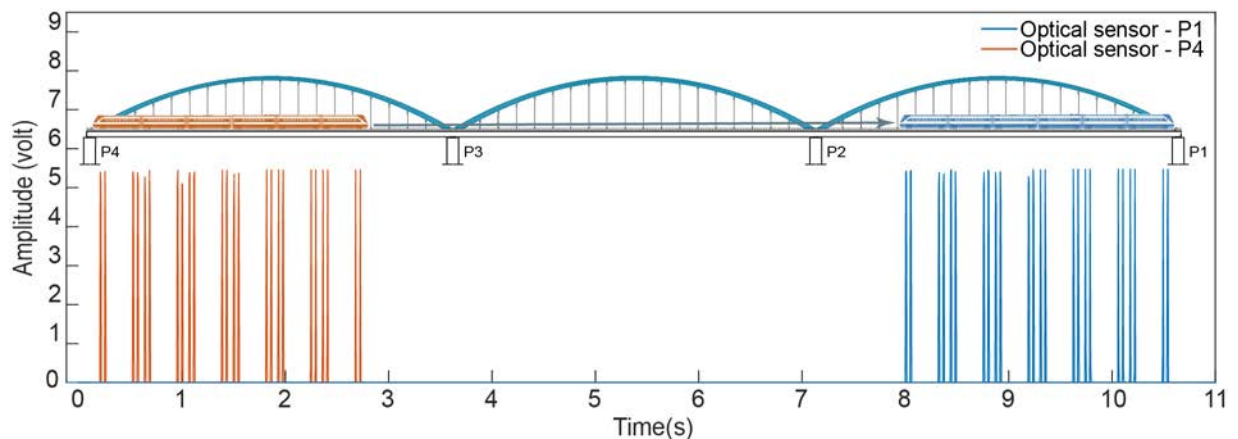


Figure 24. Axle detection based on measurements from the optical sensors during the passage of an Alfa Pendular train.

Each peak in the response of the optical sensors is generated by the passage of an axle through the optical beam. Given that the axles are easily identified, and knowing the distance (d) between the two synchronously logged optical

sensors setup, as well as the time interval (t) in which each axle crosses the laser, the train speed (v) can be seamlessly obtained as d/t .

All the dynamic analyses mentioned hereinafter were carried out for the Alfa Pendular train, which has a total length of approximately 150 m comprising four motor vehicles (BAS, BBS, BBN and BAN) and two hauled vehicles (RNB and RNH) [47]. The axle loads considered during the dynamic analysis vary between 128.8 kN and 138.4 kN, according to the loading scheme presented in Figure 25a. Typically, the Alfa Pendular train crosses the bridge near its maximum speed, which is 220 km/h. Figure 25b shows the dynamic signature of the train, which characterizes the dynamic excitation imposed by the train on the infrastructure, for a wavelength range of 4 m to 30 m, as well as the corresponding frequency response, in the range of DC to 14 Hz, for a train speed of 216 km/h. The dynamic signature depends on the axle load values and the distances between axles, and is given by the following expression [43]:

$$S_0(\lambda) = \max_{i=1, N-1} \sqrt{\left[\sum_{k=0}^i P_k \cos\left(\frac{2\pi x_k}{\lambda}\right) \right]^2 + \left[\sum_{k=0}^i P_k \sin\left(\frac{2\pi x_k}{\lambda}\right) \right]^2} \quad (1)$$

where i is the number of axles of the train, P_k is the static load of axle k , x_k is the distance between axle k and the first axle of the train, and λ is the wavelength of excitation. In Figure 25b, the most important dynamic component of this train's action is highlighted, with a wavelength of 25.9 m, associated with a regular distance between groups of four axles and a frequency of 2.362 Hz for an Alfa Pendular train at a speed of 216 km/h.

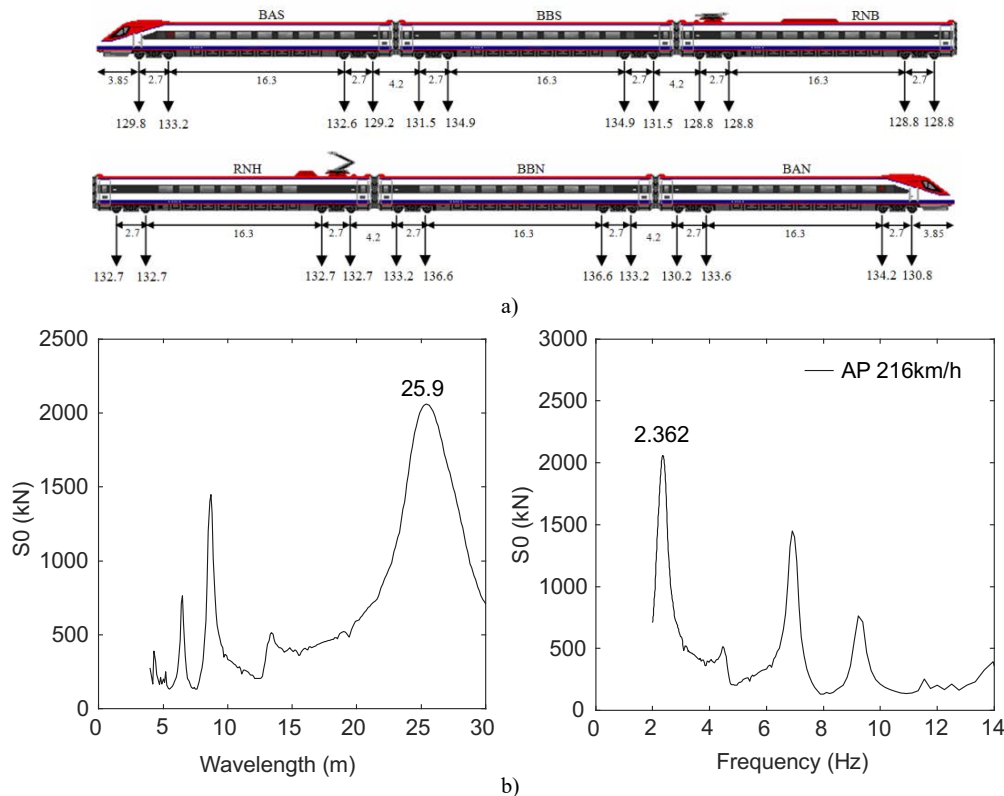


Figure 25. Alfa Pendular train: a) load scheme, b) dynamic signatures.

In order to perform the necessary dynamic analysis to predict the response of the bridge subjected to a moving train, the damping was considered using a Rayleigh damping matrix (C), which assumes the linear combination of the mass (M) and stiffness (K) matrices:

$$C = c_1 M + c_2 K \quad (2)$$

where c_1 and c_2 are the mass and stiffness proportional damping coefficients, which can be obtained by applying the least-squares method, using the following expression, that implies the prior knowledge of frequency and damping coefficient values identified in the AVT (Figure 7):

$$\xi = \frac{c_1}{2\omega} + c_2 \frac{\omega}{2} \quad (3)$$

The least-squares method finds the optimal values of the coefficients (c_1 and c_2) by minimizing the sum (S) of squared residuals, e.g., the difference between the experimental (ξ_i) and numerical (ξ_i^c) damping values of the considered mode shapes:

$$S = \sum_{i=1}^N (\xi_i - \xi_i^c)^2 = \sum_{i=1}^N (\xi_i - \frac{c_1}{4\pi f_i} - c_2 \pi f_i)^2 \quad (4)$$

The minimum value of the sum of squares was found by setting the gradient functions to zero:

$$\begin{cases} \frac{\partial S}{\partial c_1} = 0 \\ \frac{\partial S}{\partial c_2} = 0 \end{cases} \quad (5)$$

which leads to the following system of equations:

$$\begin{cases} \frac{1}{4\pi} \sum_{i=1}^N \frac{1}{f_i^2} c_1 + N\pi c_2 = \sum_{i=1}^N \frac{\xi_i}{f_i} \\ \frac{N}{4\pi} c_1 + \pi \sum_{i=1}^N f_i^2 c_2 = \sum_{i=1}^N \xi_i f_i \end{cases} \quad (6)$$

The obtained Rayleigh damping curve is illustrated in Figure 26.

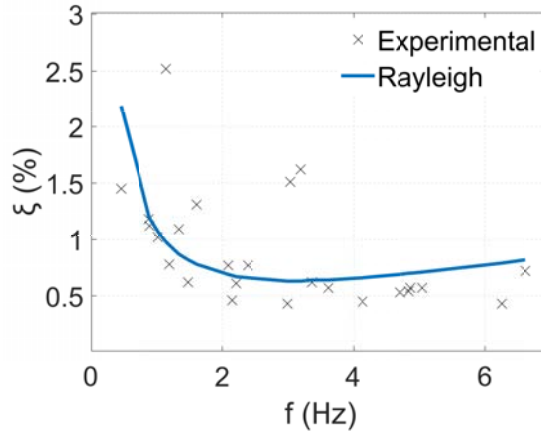


Figure 26. Relation between the damping ratio and the natural frequencies identified in the AVT.

Once again, the contact elements simulating the bearings were activated, hence, the non-linear problem was solved based on the Full Newton-Raphson method, while the dynamic analyses were performed by the Newmark direct integration method, using a moving loads methodology [10]. The integration time step (Δt) used in the analyses was 0.005 s. The analyses were concluded two seconds after the vehicle crossed the viaduct to take into account the period of free vibration of the structure.

5. Experimental validation

5.1 Validation based on ambient vibration

To validate the accuracy of the baseline numerical model in replicating the stiffness and mass distribution across the geometry of the bridge, the numerical modal properties of the Sado bridge were compared with those experimentally identified in the Ambient Vibration Test (AVT) described in section 3.2. Table 5 presents the experimental and numerical frequencies and the MAC values for 10 of the 22 vibration modes experimentally identified. The frequency Fitting Error (FE) was defined as:

$$FE_i = (f_{i,exp} - f_{i,num})/f_{i,exp} \times 100 \text{ (\%)} \quad (7)$$

where $f_{i,exp}$ and $f_{i,num}$ are the experimental and numerical frequencies obtained for mode i . The average value of the fitting error, across the identified mode shapes, is equal to 2.01%, whereas the average MAC value obtained is 0.94. The mode shapes corresponding to 10 of the 22 frequencies identified in the experimental and numerical modal analysis are plotted in Figure 27.

Table 5. Natural frequencies and MAC values.

MODE NUMBER	EXPERIMENTAL FREQ (Hz)	NUMERICAL FREQ (Hz)	FE (%)	MAC	MODE TYPE
1	0.462	0.466	0.87%	0.95	1 st LA
2	0.886	0.847	4.40%	0.95	1 st V
3	0.898	0.867	3.45%	0.98	1 st LAD
4	1.023	0.989	3.32%	0.90	2 nd V
5	1.146	1.146	0.00%	0.99	1 st LO
6	1.198	1.178	1.67%	0.98	3 rd V
7	1.343	1.316	2.01%	0.98	2 nd LA
8	1.482	1.493	-0.74%	0.91	4 th V
9	1.612	1.536	4.71%	0.86	5 th V
10	2.090	2.081	0.43%	0.93	6 th V

LA – Lateral Arches; V – Vertical, LAD – Lateral Arch & Deck coupled, LO – Longitudinal.

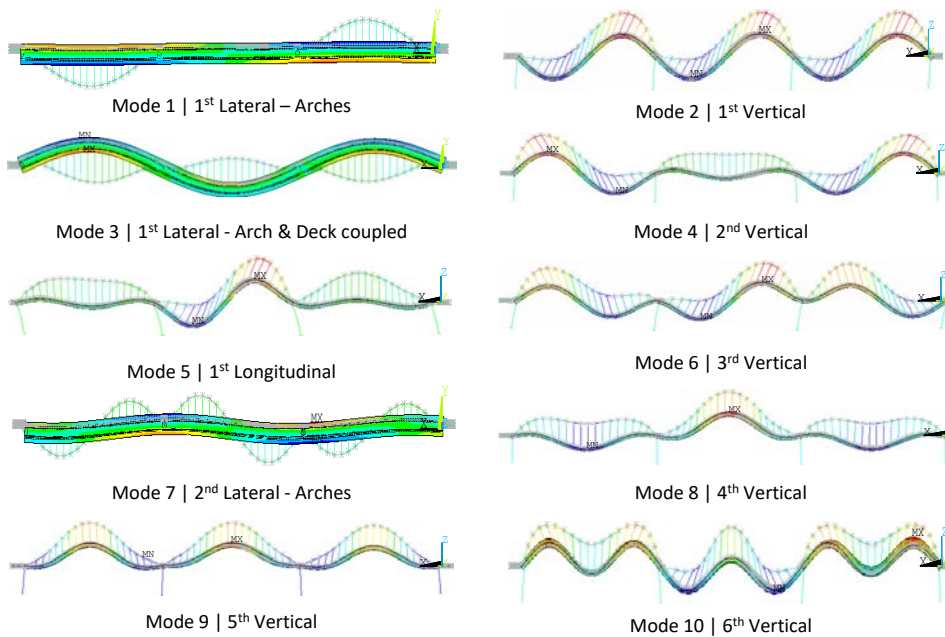


Figure 27. Numerical mode shapes.

The numerical vibration modes were identified using the materials and geometric properties defined in the design and construction phases, with the exception of the modulus of elasticity of the concrete slab, previously updated by Albuquerque et al. [38]. No abnormal behaviour or structural change needed be considered to update the numerical model. However, it is important to note that during the numerical modal analysis, the non-linear contact elements simulating the behaviour of the bearings were inactive, since they are not mobilized in an ambient vibration test.

5.2 Validation using the response to environmental loading

Validation based on environmental loading was conducted using two distinct numerical models. The first, the baseline model, was defined considering partially restrained displacements between piers P2, P3 and P4 and the deck, assuming the non-linear behaviour of the bearings and a friction coefficient equal to 1.5%, according to the data from the bearing manufacturer. The second, the updated model, was considered with fully restrained movements between piers P2 and P3 and the deck, based on the conclusions obtained in visual inspections and dynamic monitoring.

The comparison between the numerical responses (baseline and updated models) and the experimental time-history responses of the bridge over a year of thermal loads, acquired between November 2015 and November 2016, is illustrated in Figure 28 to Figure 30. Figure 28a, b show that the baseline numerical model overestimated the longitudinal displacements of the upstream bearing on pier P4. The difference between numerical and experimental data is particularly relevant during the summer months, as the temperature variation doubles that observed during winter. When conducting the same comparison using the results of non-linear static analyses performed in the updated model, a much greater correlation was obtained between numerical and experimental static responses (Figure 28). This outcome allows concluding that the longitudinal displacements of the bearings on pier P4 are influenced by the restrictions imposed on those installed on piers P2 and P3. This conclusion would hardly be obtained by analysing the experimental longitudinal displacements of P4 alone, whereas the comparison with the numerical simulation responses obtained using the environmental conditions measured on site allows the direct observation of the differences induced by structural changes. The piers where the bearings are restraint have also to resist to higher stresses than in case of healthy bearings. However, experimental information that allows for a numerical validation concerning these specific elements is not available.

Regarding the deformations of the steel box girder and the arch, Figure 29 and Figure 30 show that these elements are not significantly influenced by the defects of the bearings, since the responses obtained with the baseline numerical model are identical to those obtained with the updated numerical model. This observation allows concluding that the consequences of the restraints in the bearings to the global stresses of the arch and deck is very low. Nevertheless, a good correlation in terms of arch deformations and steel box deformations can be observed, particularly in the 1-month time-series shown in each of these figures.

The scatter plots shown in these figures for each structural response confirm the high correlation between the responses of the updated numerical model and the experimental measurements, wherein the coefficients of determination (R^2) show values of 0.981 for longitudinal displacements, 0.936 for steel box deformations and 0.903 for arch deformations.

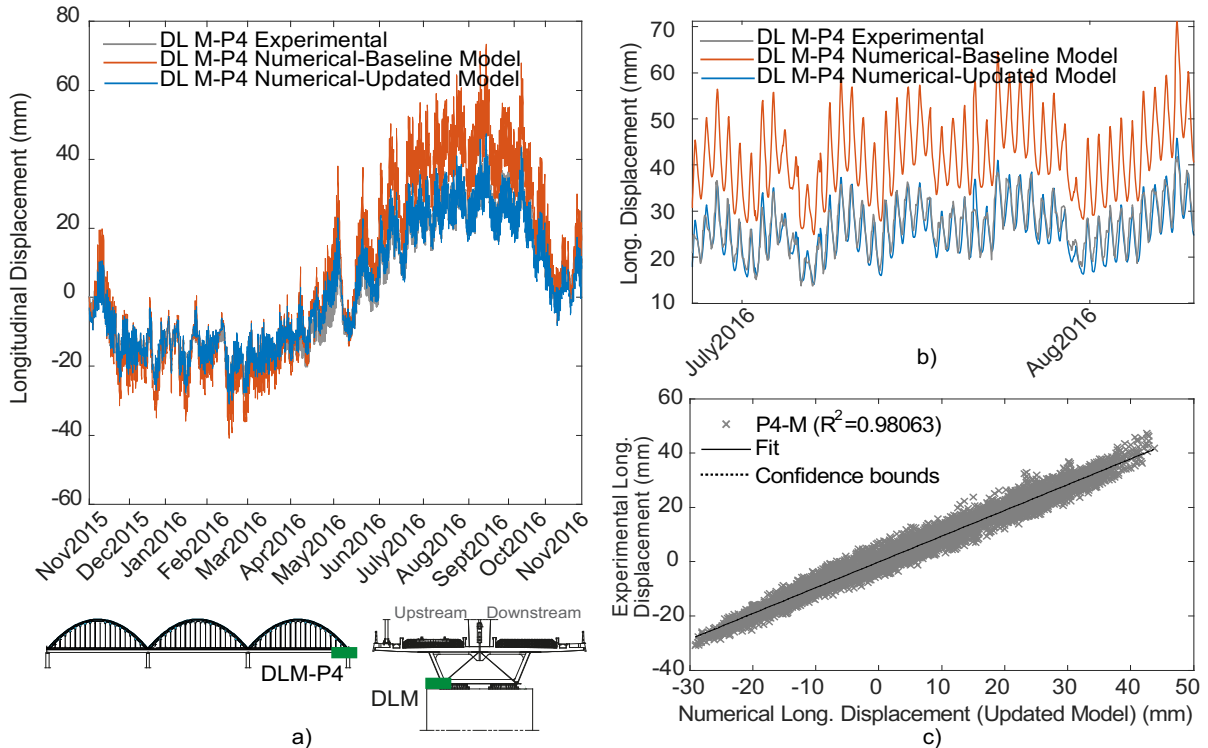


Figure 28. Numerical and experimental longitudinal displacements of the bearing on the upstream side of pier P4: a) time-history comparison, b) detail of the time-history, c) scatter plot and R^2 .

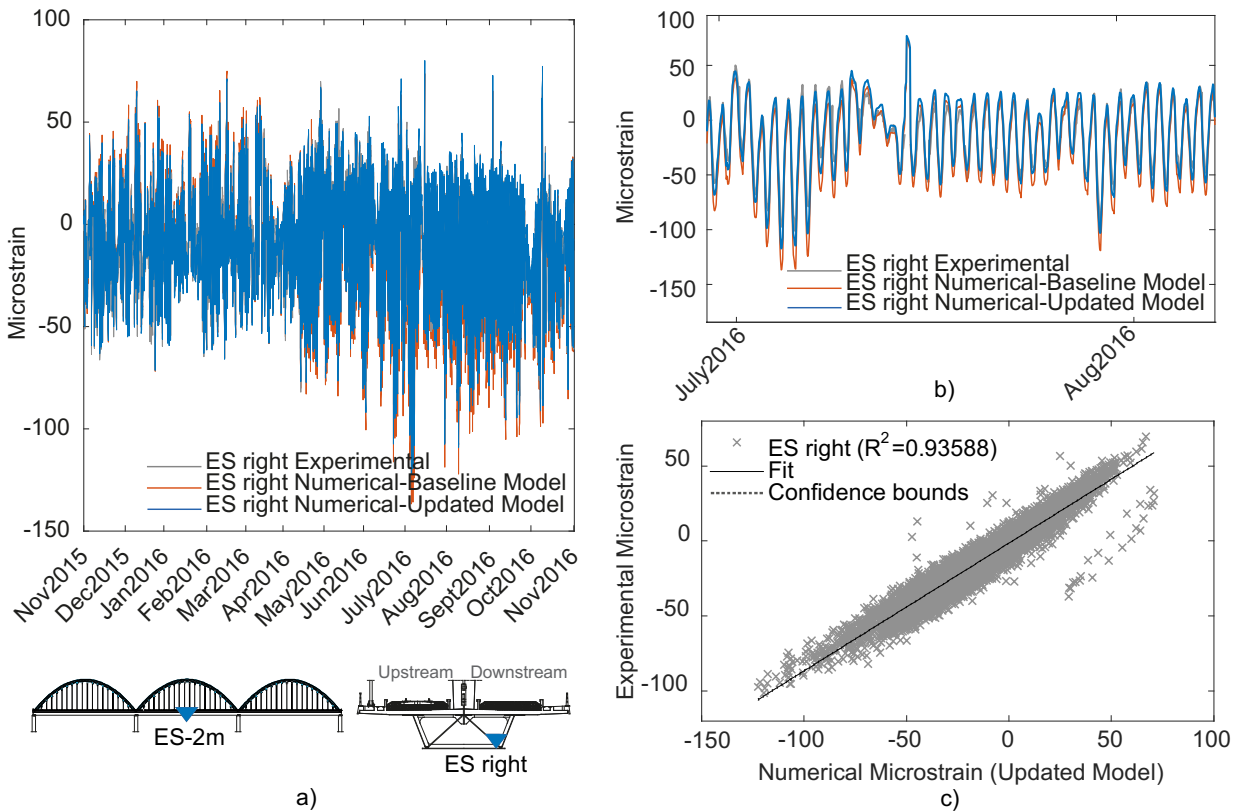


Figure 29. Numerical and experimental deformations of the steel box on the downstream side of the central deck at the mid-span section of the bridge: a) time-history comparison, b) detail of the time-history, c) scatter plot and R^2 .

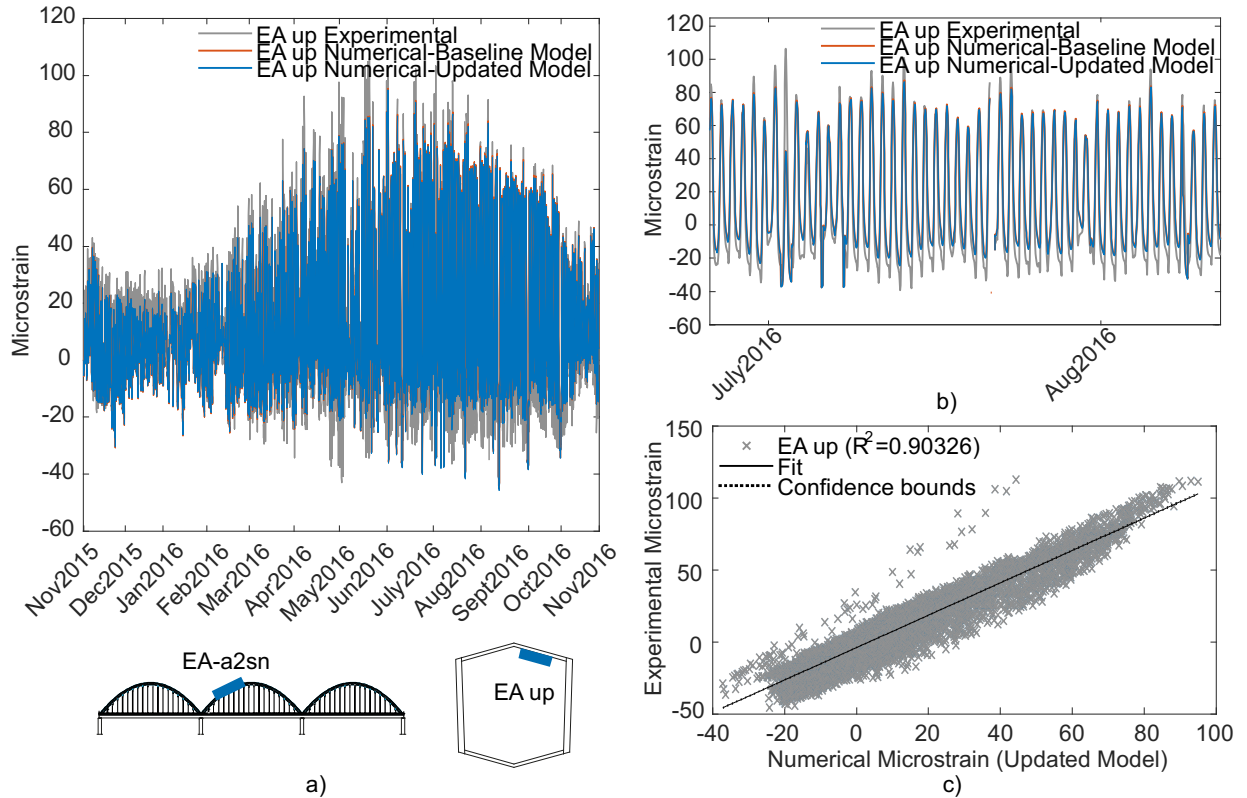


Figure 30. Numerical and experimental deformations on the upper fiber at 1/6 of the central arch section: a) time-history comparison, b) detail of the time-history, c) scatter plot and R^2 .

5.3 Validation based on the dynamic responses of the train

The analysis discussed in section 3.4 showed that the use of acceleration signals analysed in the time-domain during the passage of trains is more sensitive to slight structural changes, and, therefore, should result in a more precise validation of the model.

Numerical simulations were conducted considering the Alfa Pendular train as a set of moving loads [10] crossing the Sado bridge at 216 km/h. With this approach, in addition to considering environmental effects, as explained in the previous section, operational effects are also taken into account.

5.3.1 Analysis of displacement data

Regarding the validation of longitudinal displacements under train loads, a comparison was made between the numerical responses (baseline and updated models) and the experimental displacement time-history responses of the bridge. As for the validation under environmental loading, the baseline numerical model considered partially restrained movements between piers P2, P3, P4 and the deck, assuming the non-linear behaviour of the bearings, and the updated numerical model considered fully restrained movements between piers P2 and P3 and the deck.

As expected, Figure 31a, Figure 32a and Figure 33a, obtained for piers P2, P3 and P4, respectively, show a significant difference between numerical and experimental responses, since the experimental bearing displacements identified on piers P2 and P3 show near-null values during the passage of trains, while the numerical ones do not. Regarding pier P4, the experimental bearing displacements seem to be influenced by the restriction imposed on those installed on piers P2 and P3, as previously observed in the displacements obtained under environmental loading.

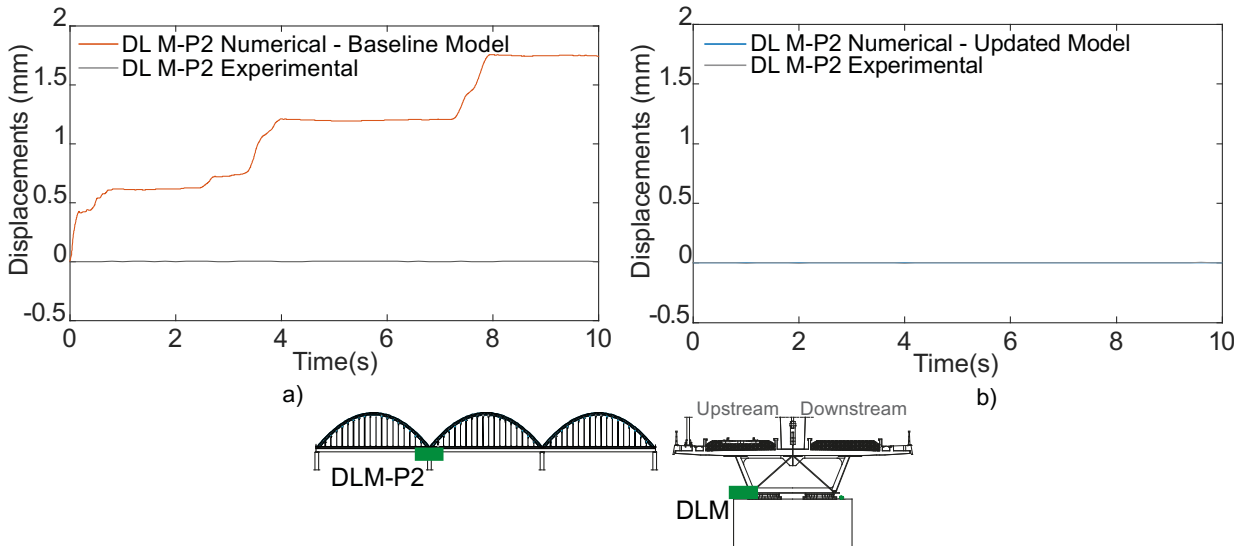


Figure 31. Numerical and experimental longitudinal displacements of the bearing on the upstream side of pier P2, with the Alfa Pendular train crossing the bridge at 216 km/h: a) baseline model, b) updated model.

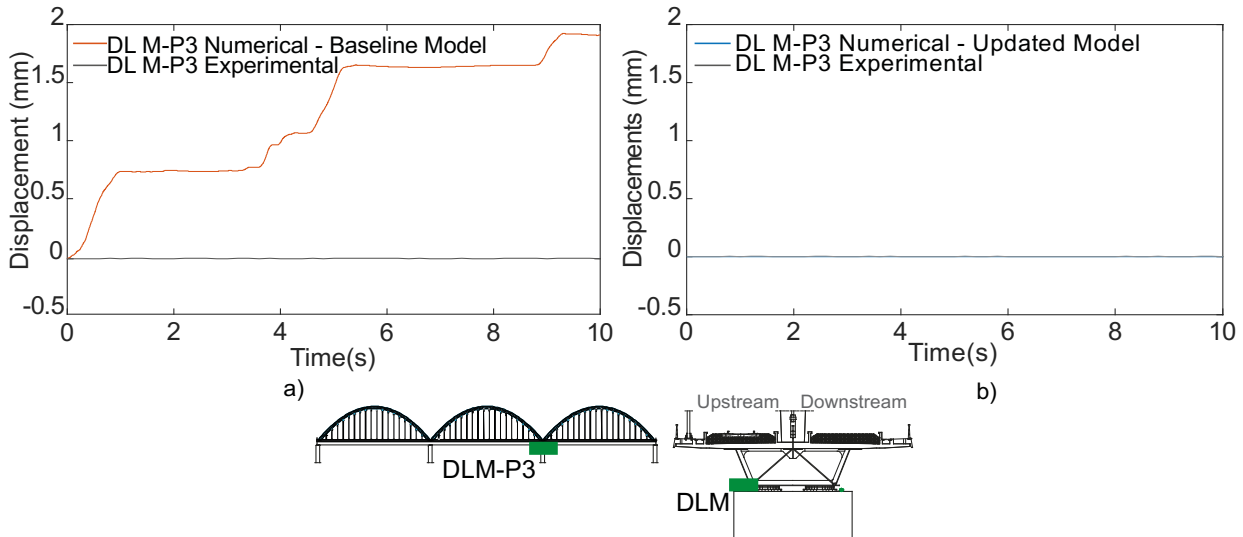


Figure 32. Numerical and experimental longitudinal displacements of the bearing on the upstream side of pier P3, with the Alfa Pendular train crossing the bridge at 216 km/h: a) baseline model, b) updated model.

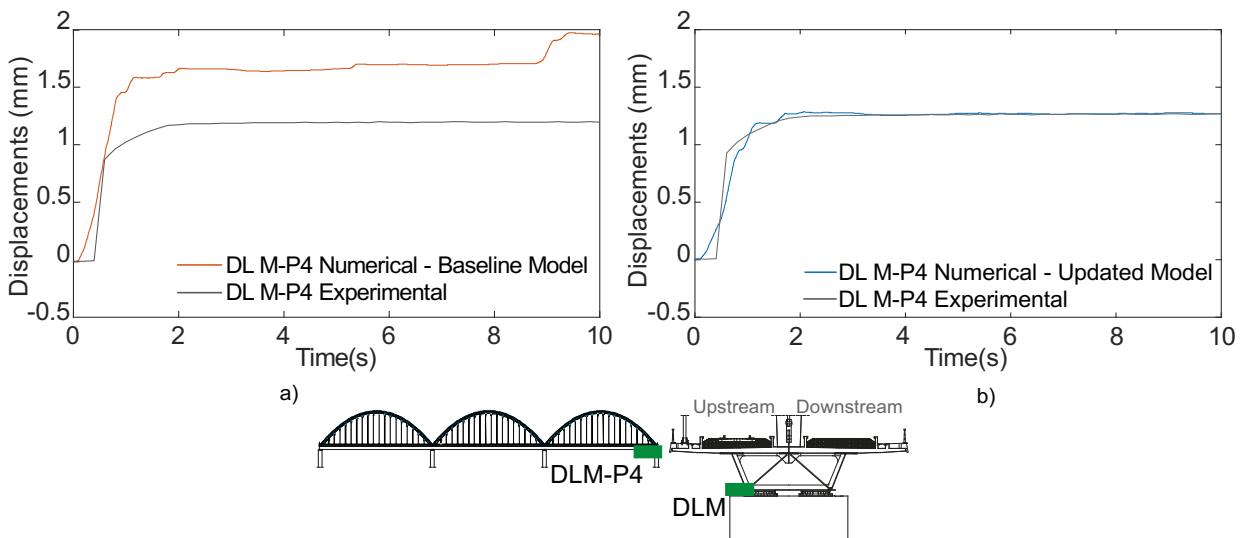


Figure 33. Numerical and experimental longitudinal displacements of the bearing on the upstream side of pier P4, with the Alfa Pendular train crossing the bridge at 216 km/h: a) baseline model, b) updated model.

The results shown in Figure 31b, Figure 32b and Figure 33b were obtained through non-linear dynamic analyses performed in the updated model but using the same experimental input data. In these plots, a very high correlation between numerical and experimental responses was achieved, not only for the near-null displacements observed on piers P2 and P3, but also, and more importantly, for the case of pier P4, where no specific model updating took place. A maximum displacement of 1.28 mm was obtained for the bearings located on pier P4 for an Alfa Pendular train crossing the Sado Bridge at 216 km/h. In a scenario in which all bearing displacements would be unrestricted, the maximum displacement on pier P4 would be approximately 2 mm, as shown in Figure 33a. It should be noted that no comparison was made for the bearings located on pier P1, since, as previously mentioned, these are mechanically fixed, according to the design of the bridge. Finally, it is important to emphasize that, using this approach, and based on the obtained results, structural changes can also be observed without the need to specifically monitor the malfunctioning elements. This is clear in Figure 33, where the restraining of the bearings on piers P2 and P3 (Figure 33b) revealed important changes when compared to the baseline model (Figure 33a).

5.3.2 Analysis of acceleration data

In addition to the validation of the longitudinal displacements measured at each bearing device, the longitudinal accelerations measured on top of each pier were also computed for the same baseline and updated numerical models. Figure 34 to Figure 37 illustrate the comparison between numerical and experimental longitudinal accelerations on piers P1, P2, P3 and P4, respectively, considering the numerical models in the baseline (a) and updated (b) conditions. The records were filtered using a low-pass digital filter with a cut-off frequency of 15 Hz.

In general, with the restraining of the bearings located on piers P2 and P3, a visible improvement was achieved, both in the time and frequency domains, as observed in the standard deviation values of the differences between the numerical and experimental responses, shown in these figures. As expected, the longitudinal accelerations acquired on piers P2 and P3 were the ones that showed the greatest differences between the responses measured in the baseline and updated models, with a decrease in the standard deviation values of 21% and 11%, respectively. In contrast, those computed for the measurements on pier P1 decreased by only 0.68%, since the deck is fixed to this pier. The bearings on pier P4 appear to be working correctly, and, as a result, the standard deviation of the differences between the numerical and experimental accelerations measured on pier P4 decreased 1.28%, considerably less than on piers P2 and P3.

Regarding the auto-spectra resulting from the longitudinal accelerations measured at each pier (Figure 34 to Figure 37), the main frequency is repeatedly 2.3 Hz, which illustrates a clear correspondence with the main peak of the dynamic signatures of the trains (Figure 25b), for both numerical models comprising unrestrained and restrained bearing devices.

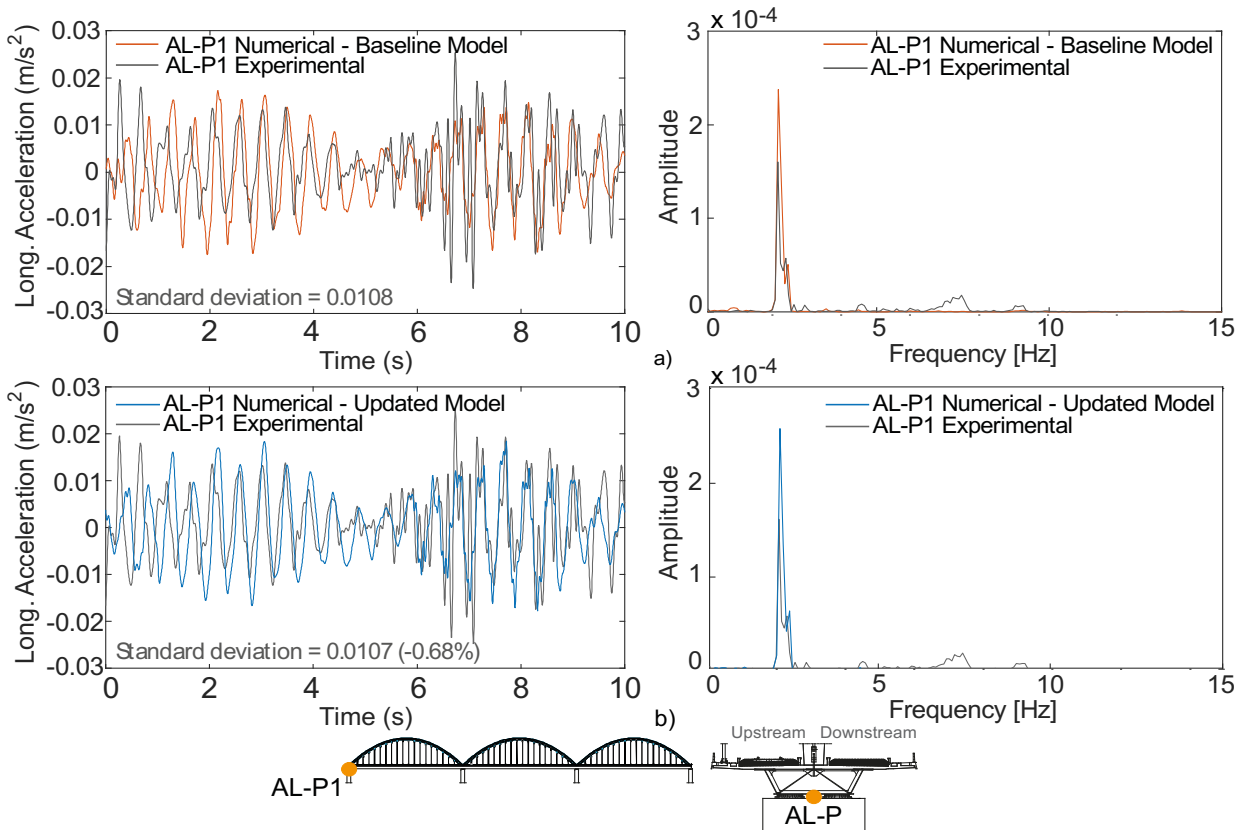


Figure 34. Numerical and experimental longitudinal accelerations and corresponding auto-spectra measured between the bearings of pier P1, with the Alfa Pendular train at 216 km/h: a) baseline model, b) updated model.

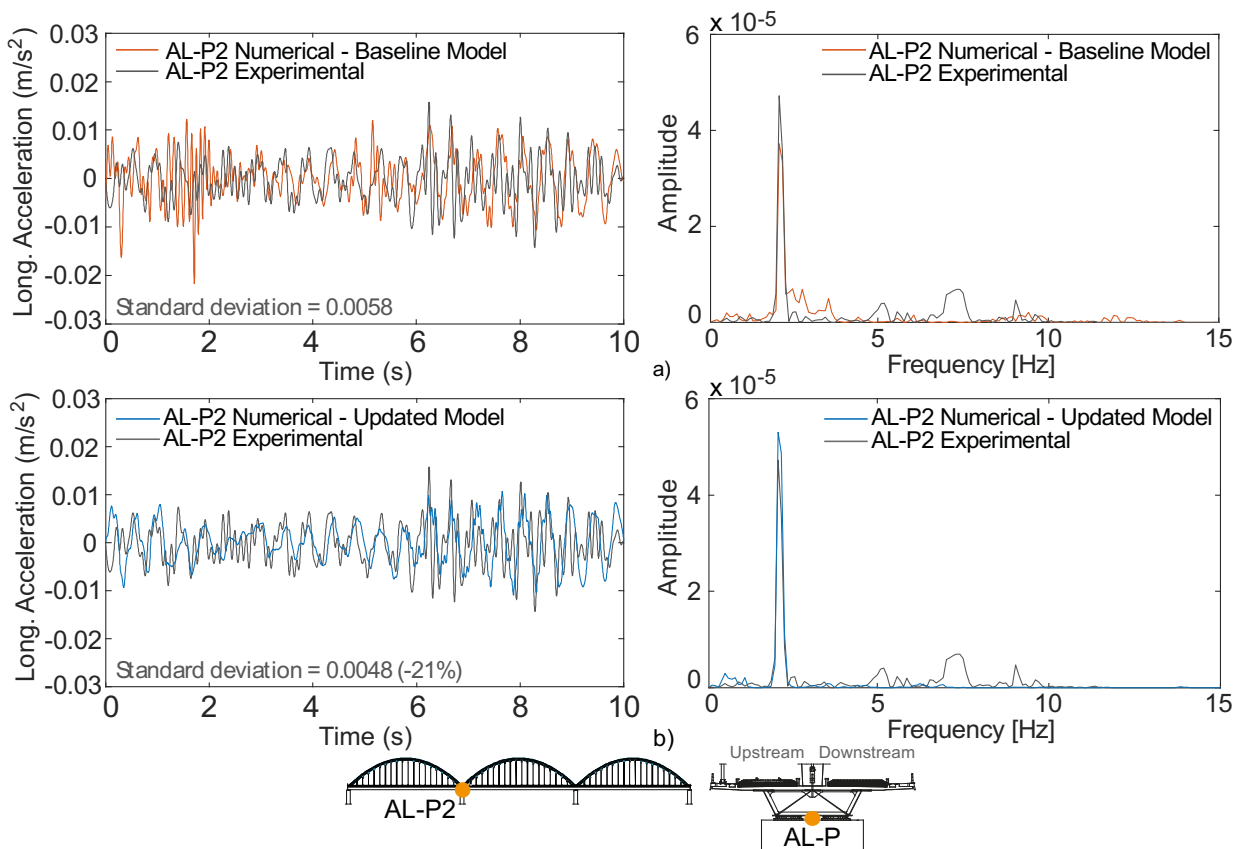


Figure 35. Numerical and experimental longitudinal accelerations and corresponding auto-spectra measured between the bearings of pier P2, with the Alfa Pendular train at 216 km/h: a) baseline model, b) updated model.

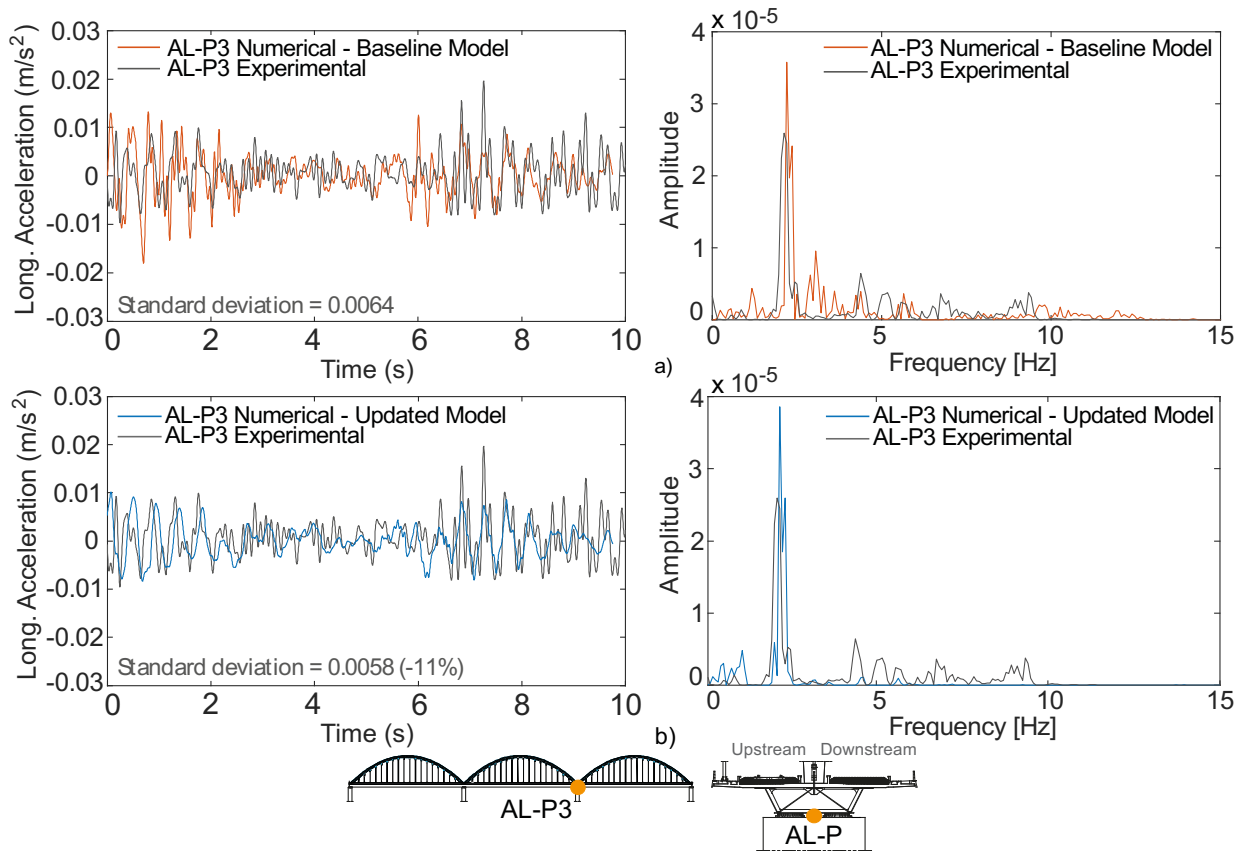


Figure 36. Numerical and experimental longitudinal accelerations and corresponding auto-spectra measured between the bearings of pier P3, with the Alfa Pendular train at 216 km/h: a) baseline model, b) updated model.

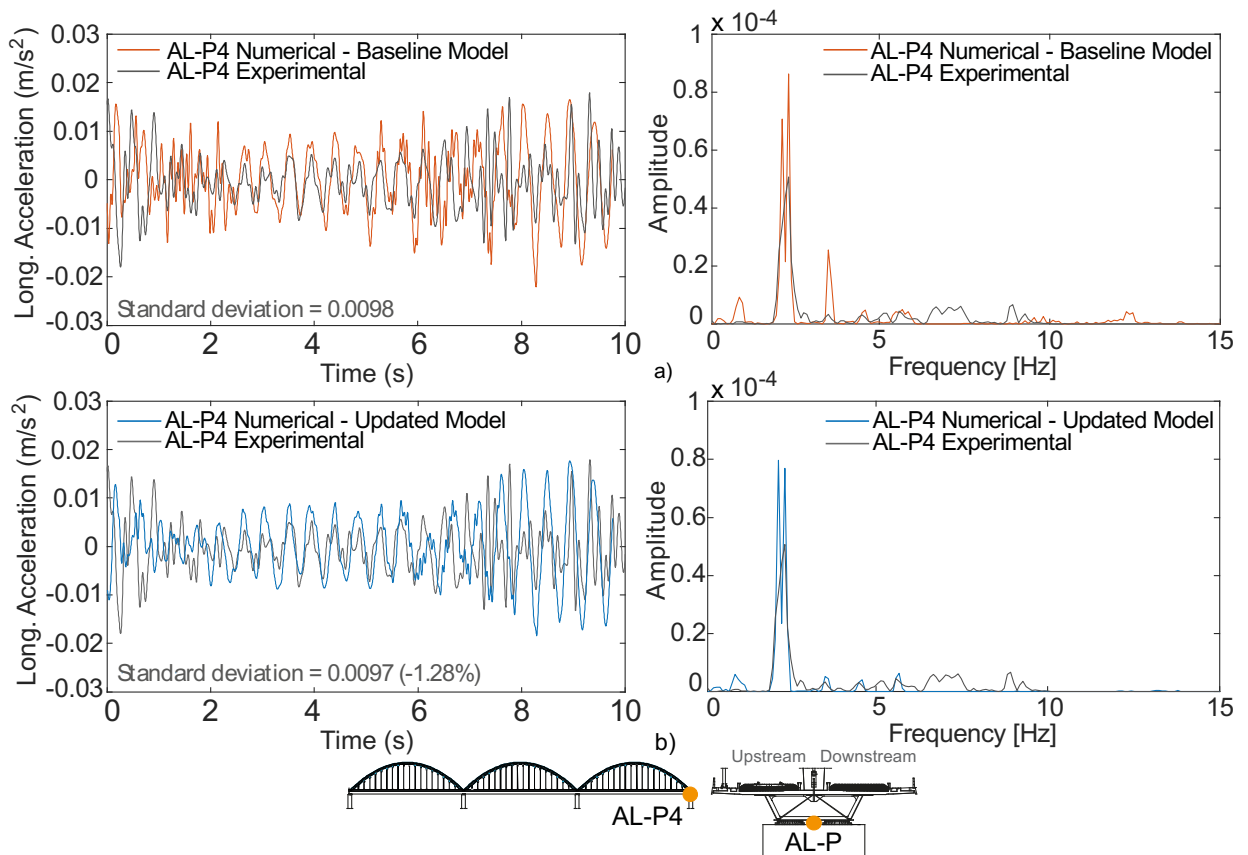


Figure 37. Numerical and experimental longitudinal accelerations and corresponding auto-spectra measured between the bearings of pier P4, with the Alfa Pendular train at 216 km/h: a) baseline model, b) updated model.

While the accelerometers installed on the piers are influenced by structural changes in the bearing devices, those installed on the bridge deck are not, since the responses obtained with the baseline numerical model coincide with those obtained with the updated numerical model (Figure 38 and Figure 39). In Figure 38 and in Figure 39 it is possible to observe the auto-spectra resulting from the vertical accelerations measured in the concrete slab and the steel box girder, respectively, where the frequencies around 2.3 Hz are related with the main modes of vibration of the structure, namely, torsion and bending modes. The preponderance of these modes is expectable since the train loading is eccentric to the single-plane bowstring-arch structure. The comparison between the experimental and numerical records of the vertical acceleration measured on the concrete slab (Figure 38) and on the steel box girder (Figure 39) in the mid-span section shows a very good agreement, both in the time and frequency domains.

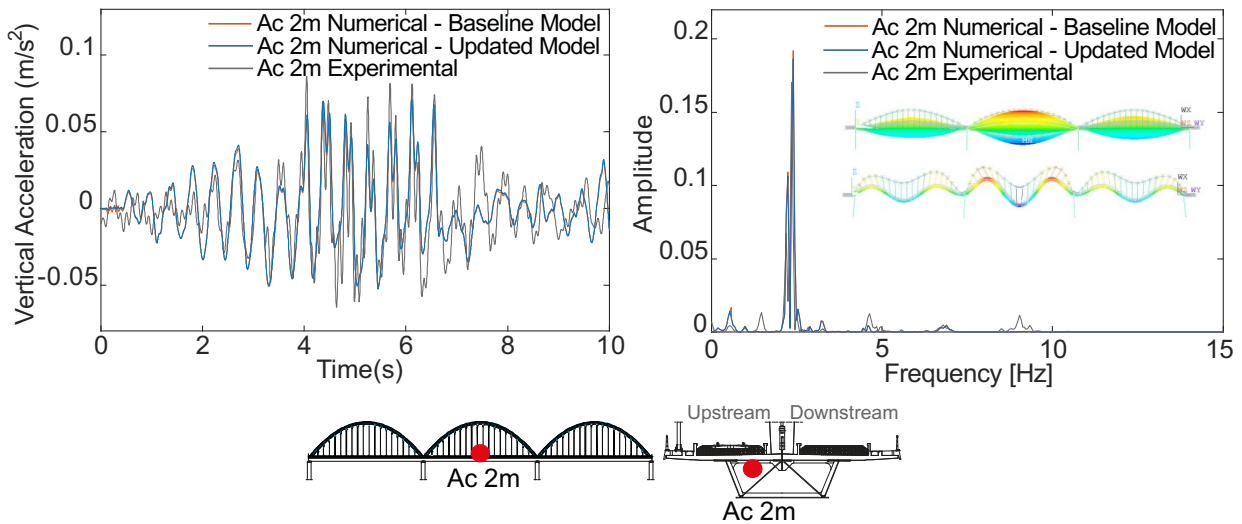


Figure 38. Numerical and experimental vertical accelerations and corresponding auto-spectra measured on the concrete slab in the mid-span section, with the Alfa Pendular train at 216 km/h.

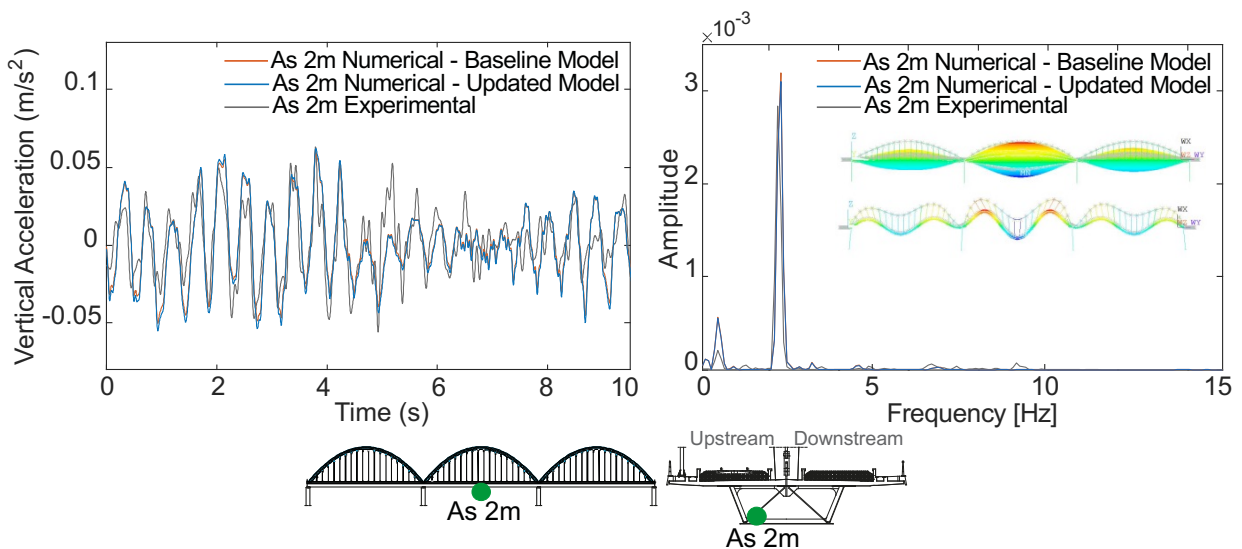


Figure 39. Numerical and experimental vertical accelerations and corresponding auto-spectra measured on the steel box in the mid-span section, with the Alfa Pendular train at 216 km/h.

6. Conclusions

This paper described the implementation of a structural health monitoring system for the progressive validation of complex non-linear FE models of bridges, performing modal analysis under ambient vibration, static analysis

based on temperature loading and dynamic analysis based on traffic loading. One of the main outcomes of this work is a validated FE model that can be used as a tool for structural health monitoring of the bridge. The case study is a bowstring-arch railway bridge comprising an extensive network of sensors, which enabled the permanent collection of static and dynamic responses, as well as the measurement of environmental and operational traffic loads.

By analysing experimental data from the ambient vibration test and static monitoring, it was possible to estimate the modal parameters, as well as the responses to important slow actions, such as temperature. However, the experimental information alone did not enable the identification of changes in the behaviour of the bearing devices. On the other hand, it was concluded that a continuous dynamic monitoring based on the analysis of traffic loading allowed the identification of changes in the structural responses, and pointed out the existence of restraints of the movements of the bearing devices on piers P2 and P3, which were also suggested by visual inspection.

The validation of the numerical model based on ambient vibration and modal analysis, revealed to be adequate to define the baseline numerical model. However, it is insufficient to perform SHM or identify structural changes, since it does not mobilize mechanical devices such as bearings (or joints).

The static validation approach based on environmental loading provided a step forward in the accuracy of the model validation, when compared to the ambient vibration analysis, due to the imposition of greater displacements on the structural elements. Based on a correlation analysis between experimental and numerical results, the restraints of the bearing devices on piers P2 and P3 were clearly identified. Without the support of a numerical model, these changes would not be easily identified using the data from the installed static monitoring system, which did not include the displacements measurement of these specific bearings. This is, in fact, another main outcome of this work, to illustrate the combined use of measurements and modelling, and the need to adapt both components over the course of a project to better understand the structural behaviour of the bridge.

The validation of the model based on dynamic monitoring under traffic loads was carried out in order to take advantage of the large displacements and vibrations imposed by this type of operational action. The model allowed analysing the influence that the restraints of the bearing devices impose to longitudinal behaviour (displacements and accelerations) of the piers, and to the vertical accelerations of the deck. It was shown that the use of numerical modelling, and its validation by comparison with SHM data, allows the detection of the full restraint of the movements of the bearing devices on piers P2 and P3 without the need to measure the longitudinal displacements at the bearings. Instead, longitudinal accelerations on top of the piers, where the bearings are located, can be measured using low cost sensors.

Based on the validated numerical model, future research work will consider the simulation of damage scenarios with different levels of severity and at several locations on the bridge. The damage detection will be based on a methodology capable of automatically extracting meaningful information related to the structural condition of railway bridges. This methodology will consider the extraction of damage-sensitive features from bridge accelerations induced by traffic loads, the normalization of these features and the classification of damages. Another matter of great concern that will be studied in a near future is the structural health monitoring of the strings and suspenders due to fatigue.

Acknowledgements

This work was financially supported by the Portuguese Foundation for Science and Technology (FCT) through the PhD scholarship SFRH/BD/93201/2013. The authors would like to acknowledge the support of the Portuguese

Road and Railway Infrastructure Manager (Infraestruturas de Portugal, I.P), the Portuguese National Laboratory for Civil Engineering (LNEC), the SAFESUSPENSE project - POCI-01-0145-FEDER-031054 (funded by COMPETE2020, POR Lisboa and FCT) and the Base Funding - UIDB/04708/2020 of the CONSTRUCT - Instituto de I&D em Estruturas e Construções - funded by national funds through the FCT/MCTES (PIDDAC).

References

1. Cantero D, González A. Bridge Damage Detection Using Weigh-in-Motion Technology. *Journal of Bridge Engineering* 2015; **20**(5): 04014078-1 to 04014078-10. DOI: 10.1061/(ASCE)BE.1943-5592.0000674.
2. Cury A, Crémona C. Assignment of structural behaviours in long-term monitoring: Application to a strengthened railway bridge. *Structural Health Monitoring* 2012; **11**(4): 422–441. DOI: 10.1177/1475921711434858.
3. Gonzalez I, Karoumi R. BWIM aided damage detection in bridges using machine learning. *Journal of Civil Structural Health Monitoring* 2015; **5**(5): 715–725. DOI: 10.1007/s13349-015-0137-4.
4. Nishio M, Marin J, Fujino Y. Uncertainty quantification of the finite element model of existing bridges for dynamic analysis. *Journal of Civil Structural Health Monitoring* 2012; **2**: 163–173. DOI: 10.1007/s13349-012-0026-z.
5. Kodikara KATL, Chan THT, Nguyen T, Thambiratnam DP. Model updating of real structures with ambient vibration data. *Journal of Civil Structural Health Monitoring Volume* 2016; **6**: 329–341.
6. Rebelo C, Simões L, Rigueiro C, Pircher M. Dynamic behaviour of twin single-span ballasted railway viaducts — Field measurements and modal identification. *Engineering Structures* 2008; **30**: 2460–2469. DOI: 10.1016/j.engstruct.2008.01.023.
7. Liu KÃ, Reynders E, Roeck G De, Lombaert G. Experimental and numerical analysis of a composite bridge for high-speed trains. *Journal of Sound and Vibration* 2009; **320**: 201–220. DOI: 10.1016/j.jsv.2008.07.010.
8. Choi J youl, Chung J seung, Kim S hee. Experimental Study on Track-Bridge Interactions for Direct Fixation Track on Long-Span Railway Bridge. *Shock and Vibration* 2019; **2019**.
9. Santos JP, Crémona C, Orcesi AD, Silveira P. Multivariate statistical analysis for early damage detection. *Engineering Structures* 2013; **56**: 273–285. DOI: 10.1016/j.engstruct.2013.05.022.
10. Ribeiro D, Calçada R, Delgado R, Brehm M, Zabel V. Finite element model updating of a bowstring-arch railway bridge based on experimental modal parameters. *Engineering Structures* 2012; **40**: 413–435. DOI: 10.1016/j.engstruct.2012.03.013.
11. Glaser SD, Tolman A. Sense of Sensing: From Data to Informed Decisions for the Built Environment. *Journal of Infrastructure Systems* 2008; **14**(1): 4–14. DOI: 10.1061/(ASCE)1076-0342(2008)14:1(4).
12. Marian Ralbovsky, Santos JP, Kwapisz M, Dallingier S, Catarino J. Damage detection based on structural response to Temperature changes and model updating. *EWSHM - European Workshop of Structural Health Monitoring*, Nantes, France: 2014.
13. Feng D, Asce SM, Feng MQ, Asce F. Model Updating of Railway Bridge Using In Situ Dynamic Displacement Measurement under Trainloads. *Journal of Bridge Engineering* 2015; **20**(2012): 1–12. DOI: 10.1061/(ASCE)BE.1943-5592.0000765.
14. Moravej H, Chan THT, Nguyen KD, Jesus A. Vibration-based Bayesian model updating of civil engineering structures applying Gaussian process metamodel. *Advances in Structural Engineering* 2019: 1–16. DOI: 10.1177/1369433219858723.
15. Weng S, Zhu HP, Xia Y, Mao L. Damage detection using the eigenparameter decomposition of substructural flexibility matrix. *Mechanical Systems and Signal Processing* 2013; **34**(1–2): 19–38. DOI: 10.1016/j.ymssp.2012.08.001.
16. Wang FL, Chan THT, Thambiratnam DP, Tan ACC, Cowled CJL. Correlation-Based Damage Detection for Complicated Truss Bridges Using Multi-Layer Genetic Algorithm. *Advances in Structural Engineering* 2012; **15**(5): 693–706.
17. Tomé ES, Pimentel M, Figueiras J. Structural response of a concrete cable-stayed bridge under thermal

- loads. *Engineering Structures Journal* 2018; **176**(April): 652–672. DOI: 10.1016/j.engstruct.2018.09.029.
18. Guo WW, Xia H, Roeck G De, Liu K. Integral model for train-track-bridge interaction on the Sesia viaduct : Dynamic simulation and critical assessment. *Computers and Structures* 2012; **112–113**: 205–216. DOI: 10.1016/j.compstruc.2012.09.001.
 19. Zhai W, Wang S, Zhang N, Gao M, Xia H, Cai C, *et al.* International Journal of Rail High-speed train – track – bridge dynamic interactions – Part II : experimental validation and engineering application. *International Journal of Rail Transportation* 2013; **1:1-2**: 25–41. DOI: 10.1080/23248378.2013.791497.
 20. Melo LRT, Ribeiro D, Calçada R, Bittencourt TN. Validation of a vertical train – track – bridge dynamic interaction model based on limited experimental data. *Structure and Infrastructure Engineering* 2020; **16**(1): 181–201. DOI: 10.1080/15732479.2019.1605394.
 21. Matsuoka K, Collina A, Somaschini C, Sogabe M. Influence of local deck vibrations on the evaluation of the maximum acceleration of a steel-concrete composite bridge for a high-speed railway. *Engineering Structures* 2019; **200**(December 2018): 109736. DOI: 10.1016/j.engstruct.2019.109736.
 22. Somaschini C, Matsuoka K, Collina A. ScienceDirect ScienceDirect Experimental analysis of a composite bridge under high-speed train passages. *Procedia Engineering* 2017; **199**: 3071–3076. DOI: 10.1016/j.proeng.2017.09.419.
 23. Cao W jun, Koh CG, Smith IFC. Enhancing static-load-test identification of bridges using dynamic data. *Engineering Structures* 2019; **186**(July 2018): 410–420. DOI: 10.1016/j.engstruct.2019.02.041.
 24. Laura M, Francesco C, Antonio F. Static and dynamic testing of highway bridges: a best practice example. *Journal of Civil Structural Health Monitoring* 2020; **10**(1): 43–56.
 25. Wang H, Li A qun, Li J. Progressive finite element model calibration of a long-span suspension bridge based on ambient vibration and static measurements. *Engineering Structures* 2010; **32**(9): 2546–2556. DOI: 10.1016/j.engstruct.2010.04.028.
 26. Rigueiro C, Rebelo C, Silva LS da. Influence of ballast models in the dynamic response of railway viaducts. *Journal of Sound and Vibration* 2010; **329**: 3030–3040. DOI: 10.1016/j.jsv.2010.02.002.
 27. Battini J marc, Ülker-kaustell M. A simple finite element to consider the non-linear influence of the ballast on vibrations of railway bridges. *Engineering Structures* 2011; **33**(9): 2597–2602. DOI: 10.1016/j.engstruct.2011.05.005.
 28. Bornet L, Andersson A, Zwolski J, Battini J marc. Influence of the ballasted track on the dynamic properties of a truss railway bridge. *Structure and Infrastructure Engineering* 2015; **11**(6): 6. DOI: 10.1080/15732479.2014.912242.
 29. ERRI D214/RP2. *Rail bridges for speeds > 200 km/h. Recommendations for calculation of bridge deck stiffness*. Utrecht, Netherlands: European Rail Research Institute (ERRI): 1999.
 30. Ülker-kaustell M, Karoumi R. Influence of non-linear stiffness and damping on the train-bridge resonance of a simply supported railway bridge. *Engineering Structures* 2012; **41**: 350–355. DOI: 10.1016/j.engstruct.2012.03.060.
 31. Malveiro J, Ribeiro D, Calçada R, Delgado R. Updating and validation of the dynamic model of a railway viaduct with precast deck. *Structure and Infrastructure Engineering* 2014; **2479**(March). DOI: 10.1080/15732479.2013.833950.
 32. Malveiro J, Ribeiro D, Sousa C, Calçada R. Model updating of a dynamic model of a composite steel-concrete railway viaduct based on experimental tests. *Engineering Structures* 2018; **164**(October 2017): 40–52.
 33. REFER. Variante de Alcácer 2010.
 34. GRID, GREISH, BEG, FERBRITAS. Variante de Alcácer: Projecto de Execução do travessamento do Rio Sado 2006.
 35. SVS. ARTEMIS Extractor Handy. *Denmark: Structural Vibration Solution* 2005(Release 3.5).
 36. Min X, Santos L. *Ensaio dinâmicos da ponte ferroviária sobre o rio sado na variante de alcácer*. Lisboa: 2011.
 37. ANSYS. Academic Research. Release 17.1 2016.
 38. Albuquerque C, Silva ALL, Jesus AMP De, Calçada R. An efficient methodology for fatigue damage

assessment of bridge details using modal superposition of stress intensity factors. *International Journal of Fatigue* 2015; **81**: 61–77. DOI: 10.1016/j.ijfatigue.2015.07.002.

39. Mijar AR, Arora JS. Review of formulations for elastostatic frictional contact problems. *Structural and Multidisciplinary Optimization* 2000; **20**(3): 167–189.
40. EN 13674-1:2003. *Railway applications — Track — Rail*. vol. 3. 2007.
41. UIC 861-3 (E). *Standard 60 Kg/m Rail Profiles - Types UIC 60 and 60E*. 3rd ed. 1969.
42. UIC 774-3-R. *Track/bridge interaction - Recommendations for calculation*. 2nd ed. Paris: 2001.
43. ERRI D 202/RP 11. *Improved knowledge of forces in CWR track (including switches): Parametric study and sensitivity analysis of CWERRI*. Utrecht: European Rail Research Institute; 1999.
44. Wu YS, Yang Y Bin. Steady-state response and riding comfort of trains moving over a series of simply supported bridges. *Engineering Structures* 2003; **25**(2): 251–265. DOI: 10.1016/S0141-0296(02)00147-5.
45. Zhai W, Wang K, Cai C. Fundamentals of vehicle-track coupled dynamics. *Vehicle System Dynamics* 2009; **47**(11): 1349–1376. DOI: 10.1080/00423110802621561.
46. Paixão A, Fortunato E, Calçada R. Transition zones to railway bridges: Track measurements and numerical modelling. *Engineering Structures* 2014; **80**: 435–443. DOI: 10.1016/j.engstruct.2014.09.024.
47. Ribeiro D, Calçada R, Delgado R, Brehm M, Zabel V. Finite-element model calibration of a railway vehicle based on experimental modal parameters. *Vehicle System Dynamics, Taylor & Francis* 2013; **51**(6): 821–856. DOI: 10.1080/00423114.2013.778416.